Effects of surface treatment on the oxidation behavior of 308L stainless steel clad in simulated PWR primary water

Tongming Cui[a,b], Xinhe Xu[a,b], Deng Pan[a,b], Jiarong Ma[a,b], Zhanpeng Lu[a,b,*], Junjie Chen[a,b], Xue Liang[a], Sergio Lozano-Perez[c], Tetsuo Shoji[d]

a. Institute of Materials, School of Materials Science and Engineering, Shanghai University, Shanghai, 200072, China

b. State Key Laboratory of Advanced Special Steels, Shanghai University, Shanghai, 200072, China

c. Department of Materials, University of Oxford, OX1 3PH, Oxford, UK

d. New Industry Creation Hatchery Center, Tohoku University, Sendai, 980-8579, Japan

*Corresponding author: Zhanpeng Lu, zplu@t.shu.edu.cn

Abstract

The properties of the oxide films grown on 308L weld metal with various surface treatments and temperatures in simulated primary water of pressurized water reactor (PWR) are studied. For the ground surface, the thickness of the inner oxide layer slightly increases with the decrease of the surface roughness. Compared with the mechanically polished surface, the higher oxidation resistance represented by a thinner inner oxide layer for the ground surface is due to the thicker fine-grained layer with high dislocations density and subgrain boundaries in the near-surface. Due to the accelerated outward diffusion of Cr at 350 ºC, Cr is found in both the inner and the outer layers of the oxide film. Nearly no Cr is found in the outer layers at 310 ºC and 325 ºC. The δ-ferrite shows a higher oxidation resistance than the γ-austenite at 310 ºC and 325 ºC, while no significant difference in the oxidation resistance can be found at 350 ºC, resulting from the thermally activated self-diffusion of Cr in ferrite. The ferrite-affected oxidation zone (FAOZ) expands with the increase in temperature from 310 ºC to 350 ºC.

Keywords: Stainless steel clad, PWR primary water, oxide film, surface state, ferrite, temperature

1. Introduction

Austenitic stainless steel (ASS) welds are widely applied as critical components in many industries attributed to the weld metals containing austenite and ferrite phases, and the well-control duplex structure is generally considered to be against corrosion and mitigate stress corrosion cracking (SCC) [1-5]. The main parameters that influence oxidation and SCC performance of austenitic alloy were identified as material and water chemistry [6-8], the type of loading [6, 7, 9], experiment temperature [9-12], and surface state [13-16]. Surface grinding or machining can lead to a severe cold-worked subsurface with considerable strain, dislocations density and deformed layer, which is usually the last stage for the fabrication of the weld joints [17]. Surface roughness, localized hardening, near-surface microstructure and high stress/strain induced by surface treatment are thought to be important factors affecting the oxidation and SCC performance of structural materials in high-temperature water environments [16, 18-27]. Many studies have been performed on the effect of different surface conditions on oxidation behavior and SCC resistance.

The oxide properties formed on alloy surfaces with different surface treatments have been studied extensively. Zhang et al. [28] suggested that the ground surface could promote the growth of a protective oxide film, and then the ground specimens showed a lower corrosion rate than the polished ones. Perez et al. [29] reported that surface finishing could produce a superficial deformation layer in the form of high density of dislocation, which would affect the oxidation behavior. Chen et al. [30] investigated the early oxidation behavior of Alloy 800H with the different surface states in 650 °C pure steam. A dual-layer Cr_2O_3 oxide scale formed on the ground Alloy 800H, the outer layer grown on mechanical polishing and electropolishing specimens was Fe_2O_3. The nanocrystalline subsurface layer in ground Alloy 800H could provide the fast Cr outward diffusion path to form a protective Cr-rich oxide layer at the metal/oxide (M/O) interface and decrease the oxidation rate. Wang et al. [20] found that the machined surface states could affect not only the thickness but also the composition of the oxide films. A more heavily cold-worked layer leads to less Cr-rich in the internal oxide layer and a more Ni-rich M/O interface. Additionally, unduly Cr-depletion below the oxide film was observed on the machined surfaces.

The SCC performance of alloy materials with different surface treatments has also been

studied. Chang et al. [24] found that machining can cause an ultrafine-grained layer and a highly deformed layer in the subsurface of 304L SS. The ultrafine-grained layer contributed to a more "uniform" oxidation and improved SCC initiation resistance of the machined samples compared to the polished ones. The research from a 316L SS showed that the subsurface ultrafine-grained layer induced by machining could inhibit crack advance, and the effect of machining-induced residual stresses on crack initiation was not significant. Furthermore, the porous internal oxide film on a machined surface was considered to be a crucial factor contributing to crack initiation [25].

However, few available data have reported the effect of the surface treatment on the corrosion and SCC behavior of the weld metals in high-temperature water [15, 17]. Due to the special microstructure and difference lattice diffusion coefficient between the ferrite and austenite phases of the weld metal, its oxidation behavior would be different from the single austenitic alloy. In addition, it has also been reported that the corrosion products or oxidation kinetics of metals and alloys can be affected by temperature [31-36]. Therefore, the oxidation behavior of austenitic weld metals in high-temperature water with the combined effects of surface states and temperatures is necessary to study. The current study applied detailed microstructure characterization to investigate the properties of oxides grown on austenite and ferrite of 308L SS cladding with different surface treatments and temperatures in a simulated PWR primary environment. The discussion is mainly focused on the effects of surface conditions, ferrite and temperatures on the oxidation behavior of 308L SS weld metal.

2. Experimental procedure

2.1. Materials and surface treatments

The material used in the current study was a nuclear grade 308L weld metal extracted from an SA508-309L/308L mock-up. The chemical composition of the 308L weld metal is as follows (in mass): 0.03% C, 0.86% Si, 1.76% Mn, 0.045% Cu, 0.002% S, 0.001% Nb, 0.096% Mo, 10.22% Ni, 19.77% Cr and Fe balance. The specimens for microstructure analysis and exposure tests were cut in the dimension of 15 × 10× 3 mm^3. Before optical microscope observation, the specimen surface was firstly polished up to 2000#, then mechanical polishing used 1-μm diamond paste and finished to electro-etched in NaOH solution. The metallographic structure of the 308L SS weld metal is shown in Fig. 1**a**. The island-like δ-ferrites (dark region)

are dispersed on the austenite matrix. Nanoindentation test was performed in a Triboindenter system (TI950, Hysitron Inc., USA) with a Berkovich type indentation tip at room temperature. A loading of 20 mN was applied and up to a maximum displacement of 600 nm. To obtain the nanohardness (GPa), a 10 × 10 area nanoindentation tests were carried out with 15 μm interval, as shown in Fig. 1**b**. The average nanohardness and Young's modulus of the 308L SS were calculated to be about 3.1 ± 0.3 GPa and 292.4 ± 9.0 GPa, respectively.

The different surface treatments are as follows: the 308L was ground use SiC emery paper to 240#, termed as 308-G240; the 308L was ground up to 600#, termed as 308-G600; the 308L was ground up to 1500#, termed as 308-G1500; the 308L was ground up to 2000#, then mechanically polished with 1-μm diamond paste, termed as 308-MP. The surface morphologies of the different surface treatment specimens were observed via Apollo 300 thermal-field emission scanning electron microscope (SEM). Surface topographies and roughness of the 308L SS weld metal specimens with different surface treatments were measured by XE7-type atomic force microscope (AFM) equipment with Park smart scan^{TM} systems. The scan region was set 20 μm × 20 μm, and the scan rate was 0.4 Hz.

2.2. Exposure tests in simulated PWR primary water

Exposure tests were conducted in a 316 SS autoclave that was equipped with a water recirculating loop system. The test solution was high-purity water containing 2.2 mg/L Li in $LiOH{\cdot}H_2O$ + 600 mg/L B in H_3BO_3. The dissolved oxygen content in the solution was kept to be below 5 μg/L, achieved through successively bubbling high-purity N_2 (≥99.999%) before hoisting up the autoclave. The solution was then purged with hydrogen gas to remove the dissolved N_2, and the DH level during the overall oxidation test was maintained at 35 cm^3 H_2/kg H_2O. The exposure tests were performed at 310 ºC for 616 h, 325 ºC for 1364 h and 350 ºC for 930 h, respectively. The summary of the sample numbers and exposure tests conditions are shown in Table 1. The specimen surfaces were cleaned with deionized water and ethanol before installing them into the autoclave.

2.3. Post-test analyses

The morphologies of the oxide film were observed by using FEI Nova Nano 450 SEM, operated at 10 kV. The cross-sectional samples preparation for transmission electron microscopy (TEM) analysis were performed via an FEI Helios 600i focused ion beam (FIB)

system. TEM bright-field (BF), high angle annular dark-field (HAADF) images and selected area electron diffraction (SAED) patterns were obtained on a JEM-2100F TEM operated at 200 kV, equipped with an energy dispersive X-ray (EDX) spectroscopy system. It is worth mentioning that the internal/external oxide interface was considered to be the original sample surface [37], and at least 3 μm width was measured to gain an internal oxide thickness.

3. Results

3.1. Microstructure of the surface treatment specimens

Figs. 2 and 3 show the surface morphologies of the 308L weld metal with the different surface treatments before exposure tests. Clear scratches with peaks and valleys are observed on the ground surfaces (Fig. 2**a-c**), while no apparent scratches and tearing-like strips can be observed on the mechanically polished surfaces (Fig. 2**d**). According to the AFM topography, the undulate of the peaks and valleys and the width of the scratches decrease with increasing the SiC emery paper grit (Fig. 3**a-d**). The surface roughness of the samples with the different surface conditions is shown in Fig. 4. The lower the emery paper grit, the larger the Ra value, and the Ra value of the mechanically polished sample is the lowest.

3.2. Oxide film formed on 308L at 310 °C for 616 h

Fig. 5 shows the oxide films formed on the 308-G240, 308-G600, 308-G1500 and 308-MP1 specimens after a 616 h exposure in hydrogenated PWR primary water. The large and medium-sized polyhedral oxide particles are distributed on the outermost layer of the oxide scale, while the compacted small ones stay in the subsurface layer. The numbers of the large and medium-sized particles on the mechanically polished specimen are the largest, while only a few large or medium-sized oxide particles can be formed on the 308-G240 specimen. Moreover, the size of the large particles on the 308-MP specimen is much larger than that on other specimens.

Figs. 6 and 7 show the TEM results of the oxide film formed on 308-G240 specimen after a 616 h exposure in hydrogenated PWR primary water. The matrix/oxide (M/O) interface is uneven. A typical double-layer oxide film is developed on the 308-G240 sample surface, Fe is enriched in the outer layer, and Cr is enriched in the inner layer. The Ni is accumulated in the M/O interface. Some deformed region rich in Cr and depletion in Ni beneath the M/O boundary is observed in Fig. 6 area maps. A clear fine-grained layer in the near-surface and some

deformed bands below the fine-grained layer of 308-G240 specimen are observed (Fig. 7**a**). The fine-grained layer measured by TEM is about 600 ± 100 nm. The SAED pattern of the fine-grained layer shows the polycrystalline characteristic, as shown in Fig. 7**c**. The inner Cr-rich oxide layer grown on 308-G240 sample surface is about 5 ± 1 nm (Fig. 7**d**). The SAED pattern of the oxide particle is identified as the face-centered cubic spinel-type crystal structure, as shown in Fig. 7**e**.

Figs. 8 and 9 show the TEM results of the oxide film grown on 308-G600 specimen after a 616 h exposure in hydrogenated PWR primary water. Sparsely Fe-rich oxide particles stay at the outer layer, and relatively dense Cr-rich oxide locates at the inner layer of the oxide film. Some micro-cracks in the substrate are observed, which may be due to the localized deformed or slip of the deformed layers during the polishing phase, as shown in Fig. 8**a**. Similar to 308-G240 specimen, the fine-grained layer with a thickness of about 400 ± 150 nm is observed in the subsurface of 308-G600 specimen, as shown in Fig. 9**a**. The diffraction ring of the fine-grained layer exhibits the polycrystalline characteristic, as shown in Fig. 9**c** SAED pattern. The thickness of the internal chromium-rich oxide layer formed on 308-G600 specimen surface measured by TEM is about 7 ± 1 nm (Fig. 9**d**). The external oxide particle shows the spinel-type crystal structure, likely in the form of (Ni, Fe)Fe_2O_4 oxide, as shown in Fig. 9**e** SAED pattern.

Figs. 10 and 11 show the TEM results of the oxide film developed on 308- G1500 specimen after a 616 h exposure in hydrogenated PWR primary water. The composition and structure of the oxide film formed on 308-G1500 sample are similar to that on 308-G240 and 308-G600 specimens, as evidenced by the TEM-EDS area maps. Compared with the former two specimens, the M/O interface is relatively even in 308-G1500 specimen, as shown in Fig. 10**a**. The fine-grained layer with the nano-size shows the polycrystalline characteristic (Fig. 11**c**), and the thickness of the fine-grained layer determined by TEM is about 200 ± 50 nm (Fig. 11**a**). The inner oxide film grown on 308-G1500 sample surface measured by TEM is about 9 ± 2 nm thick (Fig. 11**d**).

Figs. 12 and 13 show the TEM results of the oxide film grown on 308-MP1# specimen containing the phase boundary (PB) after a 616 h exposure in hydrogenated PWR primary water. The interface between the internal oxide film and external oxide can be seen clearly,

which is regarded as the specimen original surface (Fig. 12**a** and 12**b**). A typical double-layer oxide film is formed on the austenite matrix (AM) and ferrite matrix (FM). The outer oxide particles on AM are observed larger than that on FM, and the oxide formed on FM is relatively compact. Discontinuous Ni-enrichment occurs at the FM/O and AM/O interfaces, as evidenced by the Ni maps. The average thickness of the internal oxide layer upon AM measured by TEM is approximately 40 ± 5 nm. A thin internal oxide film with a thickness of less than 10 nm is observed between the FM and oxide particle (Fig. 13**c**). According to the SAED and fast Fourier transformation (FFT) pattern of the external oxide particle and internal oxide upon the FM are determined as spinel and nanocrystalline oxide, respectively.

3.3. Oxide film formed on 308L at 325 °C for 1364 h

Fig. 14 shows the SEM morphologies of oxide films on 308-MP2# sample after exposure in hydrogenated PWR primary water at 325 °C for 1364 h. The overall morphologies of the oxide film on δ-ferrite are similar to that on austenite. The oxide films on austenite and ferrite have consisted of large polyhedral oxide particles distributed on the subsurface smaller ones. However, the size and number of the oxide particles on δ-ferrite are smaller than that upon austenite. In addition, the oxide particles above the phase boundaries are slightly larger than adjacent regions.

Fig. 15 shows the TEM results of the oxide film formed on austenite in 308-MP2# sample after exposure in hydrogenated PWR primary water at 325 °C for 1364 h. A multi-layer oxide film (four layers) is observed on the austenite matrix with alternate enrichment of iron and chromium, as shown in Fig. 15**a** and 15**b**. The outer oxide particle is mainly rich in Fe and contains some Ni. The nickel is slightly enriched at the AM/O interface.

TEM results of the oxide film formed near PB on 308-MP2# sample after exposure in hydrogenated PWR primary water at 325 °C for 1364 h are shown in Figs. 16 and 17. The preferential oxidation of PB (Fig. 16**a**) could be attributed to the formation of the micro-galvanic corrosion at the δ/γ interface [38]. There are some discontinuous carbides along the PB observed. The carbide has good resistance to oxidation. The oxide film thickness on the AM is thicker than that on the FM, as shown in Figs. 16**a** and 17**b**. The thickness of the Cr-rich inner oxide layer on AM is about 85 ± 10 nm, while on FM is about 20 ± 3 nm. The average Cr content in the internal oxide film on FM is higher than that on AM. The local Ni-enrichment

is observed near the FM/O interface and PB. The ferrite shows the bcc structure is determined by the SAED pattern I in Fig. 17. The outer oxide shows the Fe_3O_4-type spinel structure, and the inner oxide shows the nanocrystalline characteristic, as shown in Fig. 17 pattern II and pattern III, respectively.

3.4. Oxide film formed on 308L at 350 °C for 930 h

Fig. 18 shows the SEM morphologies of oxide films on 308-MP3# specimen. The dispersed large oxide particle distributed on the subsurface smaller ones. With the increase of oxidation temperature to 350 ºC, the self-diffusion (likely Cr) in the ferrite phase seems to play an antioxidant role. The size of the oxide particles on ferrite and the austenite bordering the ferrite tend to be smaller than that on other regions of the austenite grains is shown in Fig. 18**c**. The ferrite-affected oxidation zone (FAOZ) becomes wider with increasing temperature. Some oxide particles upon the PB seem larger than the adjacent area (Fig. 18**c**).

Fig. 19 shows the STEM-HAADF image of the oxide film formed on 308-MP3# specimen. The semi-continuous carbides are distributed along the PB, and ferrite is embedded in the austenite matrix for about 1.5 μm depth. The thickness of the oxide film formed on AM and FM has no significant difference. The TEM-EDS results of the oxide film formed on AM of 308-MP3# specimen are shown in Fig. 20. A dual-layer oxide film has formed with a Fe-Cr rich outer layer and a Cr rich inner layer. A penetration oxidation region beneath the AM/O interface is observed with a depth of approximately 50 nm. This region is slightly rich in Ni are shown in Fig. 20**a** Ni mapping. In addition, some large voids can be found within the internal oxide film.

Fig. 21 shows the TEM-EDS results on the oxide film formed near PB (sampling location 1) on 308-MP3# specimen. The oxide film grown on AM and FM consists of two-layer, Fe-Cr is enriched in the outer layer and the Cr is enriched in the inner layer. The O/AM interface and the grain boundary are enriched in Ni, as shown in Fig. 21**a** Ni mapping and 21**c**. The thickness and the average Cr content of the internal oxide film on AM are similar to that on FM.

Fig. 22. TEM-EDS results of the oxide film formed near PB (sampling location 2) on 308-MP3# specimen. The semi-continuously carbides are observed along with the PB rich in chromium. The carbide/AM and carbide/FM interfaces seem to experience preferential oxidation of the PB (Fig. 22**a**), which is likely due to the local strain accumulation at these

regions [39]. Local Ni-enrichment at the FM/O interface and around the carbide is observed according to the Ni maps. It can be seen in the data of line 3 that the Cr content in the ferrite was slightly lower than that in the austenite. To some extent, it can be explained by the self-diffusion and rapid diffusion of chromium in ferrite in the oxidation process.

4. Discussion

4.1. Effect of surface states on oxidation and SCC of 308L SS

According to the TEM cross-sectional observation of the 308L specimens with different surface treatments, the summary of the near-surface and the properties of the oxide films on 308L SS weld metal after exposure in simulated PWR primary water is listed in Table 2. The depth of the fine-grained layer + deformed layer, dislocations density as well as subgrain boundaries number are in this order: 308-G240 > 308-G600 > 308-G1500 > 308-MP. Based on the cross-sectional characteristics, including the oxide films and substrate of 308L samples with various surface states, a schematic diagram is presented in Fig. 23. The larger the grit SiC paper, the thinner oxide on the surface. It was reported that the subsurface deformation layer produced by surface finish determines the resistance of a material of given compositions against corrosion [40]. The high density of dislocations and subgrain boundaries in the deformation layer near the surface would provide more transportation pathways for the metallic elements outward diffusion from the substrate to the metal/water interface. In addition, the strained/defected surfaces (e.g., metal strip) can offer more preferential nucleation sites for the oxides, mainly chromium-rich, which contributed to the formation of Cr-bearing protective oxide film [17, 41]. The high Cr-bearing oxide film formed on the rough surface determined the low corrosion rate of the matrix below it. Since the Cr-bearing oxide film forms faster on rough surfaces, when the Cr-bearing oxide layer is formed, it will inhibit the further transportation of the Fe and Ni, thus decreasing the oxidation rate of the metal substrate.

According to the discussion above, the rougher surfaces with a larger deformation layer are beneficial to the oxidation resistance of the 308L specimens in high-temperature water. However, SCC behavior may be quite the opposite because the prior deformed alloys, such as those cold-worked, often showed high SCC susceptibility in high-temperature water [10, 42-44]. The rougher surface has a heavy cold-worked layer and high hardness value, which would enhance SCC crack initiation and advance. Furthermore, the rougher surface with high

undulate of the peaks and valleys would lead to a poor uniformity internal oxide film on it. It was reported that the "peak" (high energy sites) of the fluctuating surface had a higher tendency to corrode than the "valley" on the rough surface [45, 46]. The undulate oxide film with considerable intrinsic strain would facilitate the crack nucleation due to the high interfacial tension within it. According to the SCC model based on the synergism of crack tip strain rate and quasi-solid state transient oxidation kinetics [47-50], the more uneven oxide film has a lower threshold strain of film degradation or rupture that contributed to the SCC crack initiation and propagation. The effects of surface conditions on the SCC behavior in high-temperature water still need to be further studied.

4.2. Effect of ferrite on the oxidation behavior of 308L SS

For the δ-ferrite, the high Cr content determined it has well oxidation resistance, as evidence of the dense and thin internal oxide layer on the ferrite. Several studies have reported that the ferrite can act as a Cr source to increase the oxidation resistance and mitigate SCC [2, 51, 52]. For the austenite, the close-packed lattice structure determined the low elements diffusion rate and the low Cr content in AM, resultant in the high oxidation rate and voids appearing within the inner oxide (Fig. 12**a**). It was reported that the formation of Cr-rich δ-ferrite can lead to Cr-depletion at the δ/γ interface, which would contribute to preferential oxidation of the PB [52], and form the large oxide particles upon the PB (Figs. 12**a**, 14**c-d**, 16**a**, and 18**c**). Xu et al. [53] found that δ-ferrite/austenite PBs are oxidized preferentially of a CF8A austenitic SS, which is attributed to the accumulation of a high level of interfacial energy and plastic damage in these regions. Moreover, the presence of micro-galvanic corrosion couple between the AM and FM is also responsible for the preferential oxidation of the PB, in which the FM with high Cr content acts as a cathode while the AM acts as the anode [53].

4.3. Effect of temperature on the oxidation behavior of 308L SS

For MP specimens, at the lower oxidation temperature (310 °C) and medium oxidation temperature (325 °C), the oxide films formed near PB have consisted of double-layer oxides, Fe-rich in the outer layer and Cr-rich in the inner layer (Figs. 12 and 16). When increasing the oxidation temperature to 350 °C, the oxide films formed near PB on both austenite and ferrite consisted of two-layer oxides, Fe-Cr-rich in the outer layer and Cr-rich in the inner layer.

It is interesting that the multi-layer oxide film is just observed on the austenite in 308-MP2#

specimen (Fig. 15), which was observed on austenitic alloy previously [40, 54]. This phenomenon is likely attributed to the different diffusion rates of the metal ions and reprecipitation. The AM below the O/M interface exhibited penetration oxidation and the number of the voids within the internal oxide film increased with increasing temperature to 350 °C (Fig. 20**a**). The higher temperature accelerated the Cr released from the metal lattice and dissolution from the inner oxide, and these "empty-sites" can not be supplemented in time due to the low chromium content of AM. It was reported that the Cr has a different diffusion rate at different temperature ranges [34], and Cr has a high affinity to the inward diffusing oxygen (vacancy), resultant in its preferential oxidation during the oxidation process. Higher temperature facilitated the Cr outward diffusion to form a protective oxide film. Due to the open lattice structure and high Cr content of the ferrite, the Cr diffuses to the surrounding austenite driven by the concentration gradient and temperature, as schematically shown in Fig. 24. It can be seen that the ferrite-affected oxidation zone (FAOZ) becomes wider with increasing oxidation temperature (Figs. 14 and 18). The temperature-driven ferrite self-diffusion can inhibit oxidation, as evidenced by the similar thickness of the oxide film formed on AM and FM, as shown in Fig. 21. The oxidized/dissolution Cr in austenite adjacent δ-ferrite could be supplied by the ferrite and attributed to the high content and lattice-diffusing coefficient of Cr in the FM [51]. The preferential oxidation of PB in 308-MP3# specimen (350 °C) was not significant (Figs. 19 and 21**a**). It is likely due to the micro-galvanic corrosion being inhibited by the Cr-diffusion from FM to adjacent AM and PB at a higher temperature.

The effect of temperature on SCC is complex in terms of temperature-related corrosion potential, pH, conductivity and hydrogen fugacity et al. For structural materials in simulated light water reactor environments, temperature-dependent SCC growth mainly includes two types, that are: crack growth increases monotonically with temperature and crack growth shows the peak at a threshold temperature [9, 10, 55-57]. However, it is reasonable to conclude that austenitic alloys with some δ-ferrite can effectively hinder crack propagation due to the special morphology, lattice structure and self-diffusion effect of δ-ferrite.

5. Conclusions

The oxidation performance of the 308L SS weld metal with various surface treatments

and temperatures in simulated PWR primary water was studied via TEM characterization of the microstructure and composition of the oxide films on these samples. Some main conclusions are as follows:

(1) For ground specimens, the surface roughness does not affect the structure of the oxide film but affects the morphologies and thickness of the oxide film. Compared with the MP surface, the ground surface has a higher oxidation resistance in terms of a thinner inner oxide layer would be ascribed to the thicker fine-grained layer with high dislocations density and subgrain boundaries in the near-surface.

(2) The special structure and high Cr-content δ-ferrite shows higher oxidation resistance than the γ-austenite at 310 ^{o}C and 325 ^{o}C, while no significant difference in the oxidation resistance can be found at 350 ^{o}C, resulting from the thermally activated self-diffusion of Cr in ferrite. The penetration oxidation tends to occur beneath the O/AM interface at a higher temperature.

(3) The effect of ferrite on inhibiting the oxidation of adjacent austenite is more significant with the increase of temperature, as indicated by the wider FAOZ at a higher temperature.

Acknowledgements

This work has been supported by Natural Science Foundation of China (NSFC No. 51771107), National Science and Technology Major Project No. 2019ZX06005002, and Independent Research and Development Project of State Key Laboratory of Advanced Special Steel, Shanghai University (SKLASS 2020-Z00).

Reference

[1] H. Abe, Y. Watanabe, Role of δ-ferrite in stress corrosion cracking retardation near fusion boundary of 316NG welds, J. Nucl. Mater. 424(1-3)(2012) 57-61.

[2] J. Wang, H. Su, K. Chen, D. Du, L. Zhang, Z. Shen, Effect of δ-ferrite on the stress corrosion cracking behavior of 321 stainless steel, Corros. Sci. 158(2019) 108079.

[3] T. Cui, X. Xu, J. Ma, Z. Lu, Y. Tang, K. Zhang, S. Yang, Z. Zhong, S. Lozano-Perez, T. Shoji, Effects of composition and microstructure on oxidation and stress corrosion cracking susceptibility of stainless steel claddings in hydrogenated PWR primary water, J. Nucl. Mater. 553(2021) 153057.

[4] Q. Xiong, H. Li, Z. Lu, J. Chen, Q. Xiao, J. Ma, X. Ru, Characterization of microstructure of A508III/309L/308L weld and oxide films formed in deaerated high-temperature water, J. Nucl. Mater. 498(2018) 227-240.

[5] J. Wang, T. Zhu, Y. Han, J. Mei, F. Xue, K. Chen, D. Du, P. L. Andresen, L. Zhang, M. Zhang, Environment assisted cracking of 308L weld metal in high temperature water, J. Nucl. Mater. 557(2021) 153275.

[6] Z. Lu, T. Shoji, F. Meng, Y. Qiu, T. Dan, H. Xue, Effects of water chemistry and loading conditions on stress corrosion cracking of cold-rolled 316NG stainless steel in high temperature water, Corros. Sci. 53(1)(2011) 247-262.

[7] Z. Lu, T. Shoji, Y. Takeda, Y. Ito, A. Kai, N. Tsuchiya, Effects of loading mode and water chemistry on stress corrosion crack growth behavior of 316L HAZ and weld metal materials in high temperature pure water, Corros. Sci. 50(3)(2008) 625-638.

[8] J. Chen, Z. Lu, Q. Xiao, X. Ru, G. Han, Z. Chen, B. Zhou, T. Shoji, The effects of cold rolling orientation and water chemistry on stress corrosion cracking behavior of 316L stainless steel in simulated PWR water environments, J. Nucl. Mater. 472(2016) 1-12.

[9] Z. Lu, T. Shoji, Y. Takeda, A. Kai, Y. Ito, Effects of loading mode and temperature on stress corrosion crack growth rates of a cold-worked type 316L stainless steel in oxygenated pure water, Corrosion 63(11) (2007) 1021-1032.

[10] K. Arioka, T. Yamada, T. Terachi, G. Chiba, Cold work and temperature dependence of stress corrosion crack growth of austenitic stainless steels in hydrogenated and oxygenated high temperature water, Corrosion. 63(2007) 1114-1123.

[11] G. Bertali, M. G. Burke, F. Scenini, N. Huin, The effect of temperature on the preferential intergranular

oxidation susceptibility of alloy 600, Metall. Mater. Trans. A. 49(2018) 1879-1894.

[12] Z. Shen, M. Meisnar, K. Arioka, S. Lozano-Perez, Mechanistic understanding of the temperature dependence of crack growth rate in alloy 600 and 316 stainless steel through high-resolution characterization, Acta Mater. 165(2019) 73-86.

[13] L. Chang, M. G. Burke, K. Mukahiwa, J. Duff, Y. Wang, F. Scenini, The effect of martensite on stress corrosion crack initiation of austenitic stainless steels in high-temperature hydrogenated water, Corros. Sci. 189(2021) 109600.

[14] Y. L. Guo, E. H. Han, J. Q. Wang, Effects of surface states on the oxidation behavior of 316LN stainless steel in high temperature pressurized water, Mater.Corros. 66(7)(2015) 670-680.

[15] Z. Que, L. Volpe, A. Toivonen, M. G. Burke, F. Scenini, U. Ehrnstén, Effects of surface treatments on environmentally-assisted cracking susceptibility of Alloy 182 in BWR environment, Corros. Sci. 188(2021) 109555.

[16] G. Han, Z. Lu, X. Ru, J. Chen, Q. Xiao, Y. Tian, Improving the oxidation resistance of 316L stainless steel in simulated pressurized water reactor primary water by electropolishing treatment, J. Nucl. Mater. 467(2015) 194-204.

[17] H. Ming, Z. Zhang, J. Wang, R. Zhu, J. Ding, J. Wang, E.H. Han, W. Ke, Effect of surface state on the oxidation behavior of welded 308L in simulated nominal primary water of PWR, Appl. Surf. Sci. 337(2015) 81-89.

[18] Q. Xiao, Z. Lu, J. Chen, J. Ma, Q. Xiong, H. Li, J. Xu, T. Shoji, Magnetoelectropolishing treatment for improving the oxidation resistance of 316L stainless steel in pressurized water reactor primary water, J. Nucl. Mater. 518(2019) 357-369.

[19] F. Scenini, R. C. Newman, R. A. Cottis, R. J. Jacko, Effect of surface preparation on intergranular stress corrosion cracking of alloy 600 in hydrogenated steam, Corrosion. 64(11)(2008) 824-835.

[20] S. Wang, Y. Hu, K. Fang, W. Zhang, X. Wang, Effect of surface machining on the corrosion behaviour of 316 austenitic stainless steel in simulated PWR water, Corros. Sci. 126(2017) 104-120.

[21] Z. Zhang, J. Wang, E.H. Han, W. Ke, Characterization of different surface states and its effects on the oxidation behaviours of alloy 690TT, J. Mater. Sci. Technol. 28(4)(2012) 353-361.

[22] W. Zhang, K. Fang, Y. Hu, S. Wang, X. Wang, Effect of machining-induced surface residual stress on initiation of stress corrosion cracking in 316 austenitic stainless steel, Corros. Sci. 108(2016)173-184.

[23] S. Cissé, L. Laffont, B. Tanguy, M.C. Lafont, E. Andrieu, Effect of surface preparation on the corrosion

of austenitic stainless steel 304L in high temperature steam and simulated PWR primary water, Corros. Sci. 56(2012)209-216.

[24] L. Chang, L. Volpe, Y. L. Wang, M. G. Burke, A. Maurotto, D. Tice, S. Lozano-Perez, F. Scenini, Effect of machining on stress corrosion crack initiation in warm-forged type 304L stainless steel in high temperature water, Acta Mater. 165(2019)203-214.

[25] L. Chang, M. G. Burke, F. Scenini, Stress corrosion crack initiation in machined type 316L austenitic stainless steel in simulated pressurized water reactor primary water, Corros. Sci. 138(2018)54-65.

[26] L. Chang, M. G. Burke, F. Scenini, Understanding the effect of surface finish on stress corrosion crack initiation in warm-forged stainless steel 304L in high-temperature water, Scripta Mater. 164(2019)1-5.

[27] L. Chang, K. Mukahiwa, L. Volpe, F. Scenini, Effect of machining on oxide development in type 316L stainless steel in high-temperature hydrogenated water, Corros. Sci. 186(2021) 109444.

[28] Z. Zhang, J. Wang, E.H. Han, W. Ke, Analysis of surface oxide films formed in hydrogenated primary water on alloy 690TT samples with different surface states, J. Mater. Sci. Technol. 30(12)(2014) 1181-1192.

[29] S. Lozano-Perez, K. Kruska, I. Iyengar, T. Terachi, T. Yamada, The role of cold work and applied stress on surface oxidation of 304 stainless steel, Corros. Sci. 56(2012) 78-85.

[30] J. Chen, C. Jang, Q. Xiao, H. B. Lee, C. Kim, S. H. Kim, J. H. Shin, G. Obulan Subramanian, Effect of surface conditions and alloying elements on the early oxidation behaviour of two austenitic alloys in the pure steam environment, Appl. Surf. Sci. 563(2021) 150314.

[31] H. Sun, X. Wu, E.H. Han, Effects of temperature on the oxide film properties of 304 stainless steel in high temperature lithium borate buffer solution, Corros. Sci. 51(12)(2009) 2840-2847.

[32] R. Mendonça, R. W. Bosch, W. Van Renterghem, M. Vankeerberghen, C. de Araújo Figueiredo, Effect of temperature and dissolved hydrogen on oxide films formed on Ni and Alloy 182 in simulated PWR water, J. Nucl. Mater. 477(2016) 280-291.

[33] C. Lukac, J. B. Lumsden, S. Smialowska, R. W. Staehle, Effects of temperature on the kinetics of passive film growth on iron, J. Electrochem. Soc. 122(1975) 1571-1579.

[34] J. Wang, J. Wang, H. Ming, Z. Zhang, E.H. Han, Effect of temperature on corrosion behavior of alloy 690 in high temperature hydrogenated water, J. Mater. Sci. Technol. 34(8)(2018) 1419-1427.

[35] Q. Xiao, Z. Lu, J. Chen, M. Yao, Z. Chen, A. Ejaz, The effects of temperature and aeration on the corrosion of A508III low alloy steel in boric acid solutions at 25–95 °C, J. Nucl. Mater. 480(2016) 88-99.

[36] Z. Zhu, H. Xu, D. Jiang, X. Mao, N. Zhang, Influence of temperature on the oxidation behaviour of a ferritic-martensitic steel in supercritical water, Corros. Sci. 113(2016) 172-179.

[37] J. Robertson, The mechanism of high temperature aqueous corrosion of stainless steels, Corros. Sci. 32(4)(1991) 443-465.

[38] H. M. Shalaby, Failure investigation of 321 stainless steel pipe to flange weld joint, Eng. Fail. Anal. 80(2017) 290-298.

[39] K. Chen, J. Wang, Z. Shen, D. Du, X. Guo, L. Zhang, P. L. Andresen, Effect of intergranular carbides on the cracking behavior of cold worked alloy 690 in subcritical and supercritical water, Corros. Sci. 164(2020) 108313.

[40] F. Huang, J. Wang, E.H. Han, W. Ke, Microstructural characteristics of the oxide films formed on Alloy 690 TT in pure and primary water at 325°C, Corros. Sci. 76(2013) 52-59.

[41] S. Ghosh, M. K. Kumar, V. Kain, High temperature oxidation behavior of AISI 304L stainless steel-Effect of surface working operations, Appl. Surf. Sci. 264(2013) 312-319.

[42] T. Shoji, G. F. Li, J. H. Kwon, S. Matsushima, Z. P. Lu, Quantification of yield strength effects on IGSCC of austenitic stainless steels in high temperature waters, in: Proc. 11th Int. Conf. Environ. Degradation of Materials in Nuclear Power Systems–Water Reactors. ANS(2003) 834-843.

[43] K. Arioka, T. Yamada, T. Terachi, G. Chiba, Influence of carbide precipitation and rolling direction on intergranular stress corrosion cracking of austenitic stainless steels in hydrogenated high-temperature water, Corrosion. 62(7)(2006) 568-575.

[44] L. Tribouilloy, F. Vaillant, T. Couvant, J. M. Boursier, Y. Rouillon, C. Amzallag, J. M. Olive, M. Puiggali, L. Legras, Stress corrosion cracking of cold-worked austenitic stainless steels in PWR environments, in: Proc 13th Int. Conf. Environ. Degradation of Materials in Nuclear Power Systems–Water Reactors. CDROM (2007)

[45] W. Li, D. Y. Li, Variations of work function and corrosion behaviors of deformed copper surfaces, Appl. Surf. Sci. 240(1-4)(2005) 388-395.

[46] W. Li, D. Y. Li, Influence of surface morphology on corrosion and electronic behavior, Acta Mater. 54(2)(2006) 445-452.

[47] T. Shoji, Z. Lu, H. Murakami, Formulating stress corrosion cracking growth rates by combination of crack tip mechanics and crack tip oxidation kinetics, Corros. Sci. 52(3)(2010) 769-779.

[48] Z. Lu, T. Shoji, H. Xue, C. Fu, Deterministic formulation of the effect of stress intensity factor on PWSCC

of Ni-base alloys and weld metals, J. Press. Vessel Technol. 135(2013) 021402-1-9.

[49] F. P. Ford, Quantitative prediction of environmentally assisted cracking, Corrosion. 52(1996) 375-395.

[50] P. L. Andresen, F. P. Ford, Life prediction by mechanistic modeling and system monitoring of environmental cracking of iron and nickel alloys in aqueous systems, Mat. Sci. Eng. A 103(1988) 167-184.

[51] G. Bai, S. Lu, D. Li, Y. Li, Intergranular corrosion behavior associated with delta-ferrite transformation of Ti-modified Super 304H austenitic stainless steel, Corros. Sci. 90(2015) 347-358.

[52] T. Cui, H. Dong, X. Xu, J. Ma, Z. Lu, Y. Tang, D. Pan, S. Lozano-Perez, T. Shoji, Hydrogen-enhanced oxidation of ferrite phase in stainless steel cladding and the contribution to stress corrosion cracking in deaerated high temperature water, J. Nucl. Mater. 557(2021) 153209.

[53] Y. Xu, H. Jing, L. Xu, Y. Han, L. Zhao, Effect of δ-ferrite on stress corrosion cracking of CF8A austenitic stainless steels in a simulated pressurised water reactor environment, J. Mater. Res. Technol. 8(6)(2019) 6420-6426.

[54] Z. Zhang, J. Wang, E.H. Han, W. Ke, Influence of dissolved oxygen on oxide films of Alloy 690TT with different surface status in simulated primary water, Corros. Sci. 53(2011) 3623-3635.

[55] K. Arioka, T. Yamada, T. Miyamoto, M. Aoki, Intergranular stress corrosion cracking growth behavior of Ni-Cr-Fe alloys in pressurized water reactor primary water, Corrosion. 70(7)(2014) 695-707.

[56] K. Arioka, T. Yamada, T. Terachi, T. Miyamoto, Dependence of stress corrosion cracking for cold-worked stainless steel on temperature and potential, and role of diffusion of vacancies at crack tips, Corrosion. 64(9)(2008) 691-706.

[57] Z. Lu, Y. Takeda, T. Shoji, Some fundamental aspects of thermally activated processes involved in stress corrosion cracking in high temperature aqueous environments, J. Nucl. Mater. 383(1-2)(2008) 92-96.

Figure captions

Fig. 1. (a) Optical image of the 308L weld metal after electro-etched in NaOH solution, (b) Nanoindentation test area image of the 308L weld metal.

Fig. 2. SEM surface morphology of the 308L SS specimens with different surface treatment: (a) 308-G240, (b) 308-G600, (c) 308-G1500, (d) 308-MP.

Fig. 3. AFM Topography of the 308L SS specimens with different surface treatment: (a) 308-G240, (b) 308-G600, (c) 308-G1500, (d) 308-MP.

Fig. 4. Roughness values of the 308L SS specimens with different surface treatments.

Fig. 5. SEM morphologies of the 308L SS specimens after exposure in hydrogenated simulated PWR primary water at 310 ºC for 616 h: (a) 308-G240, (b) 308-G600, (c) 308-G1500, (d) 308-MP1#.

Fig. 6. TEM-EDS results of the oxide film formed on 308-G240 specimen after exposure in hydrogenated PWR primary water at 310 ºC for 616 h: (a) STEM-HAADF image of the oxide film and the corresponding EDS maps, (b) EDS line scan profile of the oxide film shown in (a).

Fig. 7. (a) TEM-BF image of the subsurface and oxide film formed on 308-G240 specimen after exposure in hydrogenated PWR primary water at 310 ºC for 616 h, (b) High magnification TEM-BF image of the fine grained layer marked by the red rectangle dash box shown in (a), (c) SAED image of the fine grained layer as the red circle shown in (a), (d) High resolution TEM image of the outer/inner oxide/matrix interface, (e) SAED pattern of the outer oxide particle.

Fig. 8. TEM-EDS results of the oxide film formed on 308-G600 specimen after exposure in hydrogenated PWR primary water at 310 ºC for 616 h: (a) STEM-HAADF image of the oxide film and the corresponding EDS maps, (b) EDS line scan profile of the oxide film shown in (a).

Fig. 9. (a) TEM-BF image of the subsurface and oxide film formed on 308-G600 specimen after exposure in hydrogenated PWR primary water at 310 ºC for 616 h, (b) High magnification TEM-BF image of the fine grained layer marked by the red rectangle dash box shown in (a), (c) SAED image of the fine grained layer as the red circle shown in (a), (d) High resolution TEM image of the outer/inner oxide/matrix interface, (e) SAED pattern of the outer oxide particle.

Fig. 10. TEM-EDS results of the oxide film formed on 308-G1500 specimen after exposure in hydrogenated PWR primary water at 310 ºC for 616 h: (a) Low magnification STEM-HAADF image of the oxide film, (b) High magnification STEM-HAADF image of the oxide film and the corresponding EDS area maps, (c) EDS line scan profile of the oxide film shown in (a) as line 1, (c) EDS line scan profile

of the oxide film shown in (a) as line 2.

Fig. 11. (a) TEM-BF image of the subsurface and oxide film formed on 308-G1500 specimen after exposure in hydrogenated PWR primary water at 310 ºC for 616 h, (b) High magnification TEM-BF image of the fine grained layer marked by the red rectangle dash box shown in (a), (c) SAED image of the fine grained layer as the red circle shown in (a), (d) High resolution TEM image of the outer/inner oxide/matrix interface, (e) SAED pattern of the outer oxide particle.

Fig. 12. TEM-EDS results of the oxide film formed near PB on 308-MP1# specimen after exposure in hydrogenated PWR primary water at 310 ºC for 616 h: (a) STEM-HAADF image of the oxide film formed near the phase boundary and the corresponding EDS maps, (b) STEM-HAADF image of the oxide film formed on austenite, (c) EDS line scan profile of the oxide film on austenite shown in (b), (d) STEM-HAADF image of the oxide film formed on ferrite, (e) EDS line scan profile of the oxide film on ferrite shown in (d).

Fig. 13. (a) TEM-BF image of the oxide film formed on austenite in 308-MP1# specimen after exposure in hydrogenated PWR primary water at 310 ºC for 616 h, (b) TEM-BF image of the oxide film on ferrite, (c) HRTEM image of the oxide formed on ferrite marked by the white rectangle dash box shown in (b). I shows the SAED pattern of the outer oxide particle on ferrite, II shows the FFT pattern of the inner oxide on ferrite.

Fig. 14. SEM morphologies of oxide films on 308-MP2# specimen after exposure in hydrogenated PWR primary water at 325 ºC for 1364 h: (a) (c) SE images, (b) (d) BSE images.

Fig. 15. TEM results of the oxide film formed on austenite in 308-MP2# specimen after exposure in hydrogenated PWR primary water at 325 ºC for 1364 h: (a) STEM-HAADF image of the oxide film on austenite and the corresponding EDS maps, (b) EDS line scan profile of the oxide film on austenite shown in (a).

Fig. 16. TEM-EDS results of the oxide film formed near phase boundary on 308-MP2# specimen after exposure in hydrogenated PWR primary water at 325 ºC for 1364 h: (a) STEM-HAADF image of the oxide film formed near the phase boundary and the corresponding EDS maps, (b) EDS line scan profile of the oxide film on austenite shown in (a), (c) EDS line scan profile of the oxide film on ferrite shown in (a).

Fig. 17. (a) TEM-BF image of the ferrite and oxide films formed near phase boundary on 308-MP2# specimen after exposure in hydrogenated PWR primary water at 325 ºC for 1364 h, (b) TEM-DF image

of the ferrite, (c) High magnification TEM-BF image of the PB and oxide film marked by the white rectangular box shown in (a). I shows the SAED pattern of the ferrite, II shows the SAED pattern of the outer oxide on austenite, III shows the FFT pattern of the inner oxide on austenite.

Fig. 18. SEM morphologies of oxide films on 308-MP3# specimen after exposure in hydrogenated PWR primary water at 350 ºC for 930 h: (a) (b) SE image, (c) BSE image.

Fig. 19. Low magnification STEM-HAADF image of the oxide film formed on 308-MP3# specimen after exposure in hydrogenated PWR primary water at 350 ºC for 930 h.

Fig. 20. TEM-EDS results of the oxide film formed on austenite of 308-MP3# specimen after exposure in hydrogenated PWR primary water at 350 ºC for 930 h: (a) STEM-HAADF image of the oxide film on austenite and the corresponding EDS maps, (b) EDS line scan profile of the oxide film on austenite shown in (a).

Fig. 21. TEM-EDS results of the oxide film formed near phase boundary (sampling location 1) on 308-MP3# specimen after exposure in hydrogenated PWR primary water at 350 ºC for 930 h: (a) STEM-HAADF image of the oxide film formed near the phase boundary and the corresponding EDS area maps, (b) EDS line scan profile of the oxide film on ferrite shown in (a), (c) EDS line scan profile of the oxide film on austenite shown in (a).

Fig. 22. TEM-EDS results of the oxide film formed near phase boundary (sampling location 2) on 308-MP3# specimen after exposure in hydrogenated PWR primary water at 350 ºC for 930 h: (a) STEM-HAADF image of the oxide film formed near the phase boundary and the corresponding EDS area maps, (b) EDS line scan profile of the oxide film on ferrite shown in (a) as line 1, (c) EDS line scan profile of the oxide film on austenite shown in (a) as line 2, EDS line scan profile across the austenite-ferrite-carbide shown in (a) as line 3.

Fig. 23. Schematic diagram of the oxide films grown on a 308L SS cladding (not including PB) with different surface treatments: (a) 308-G240 specimen, (b) 308-G600 specimen, (c) 308-G1500 specimen, (d) 308-MP1#.

Fig. 24. Schematic diagram of the oxide films grown on mechanical polished 308L SS cladding (including PB) with different temperature: (a) 308-MP1# specimen, (b) 308-MP2# specimen, (c) 308-MP3# specimen. The thickness of the inner oxide layer is arbitrary.

Table captions

Table 1. Test conditions employed for the oxidation of 308L SS weld metal in simulated PWR primary water.

Table 2. Summary of the near-surface and oxide films properties of 308L SS weld metal with various surface states in simulated PWR primary water.

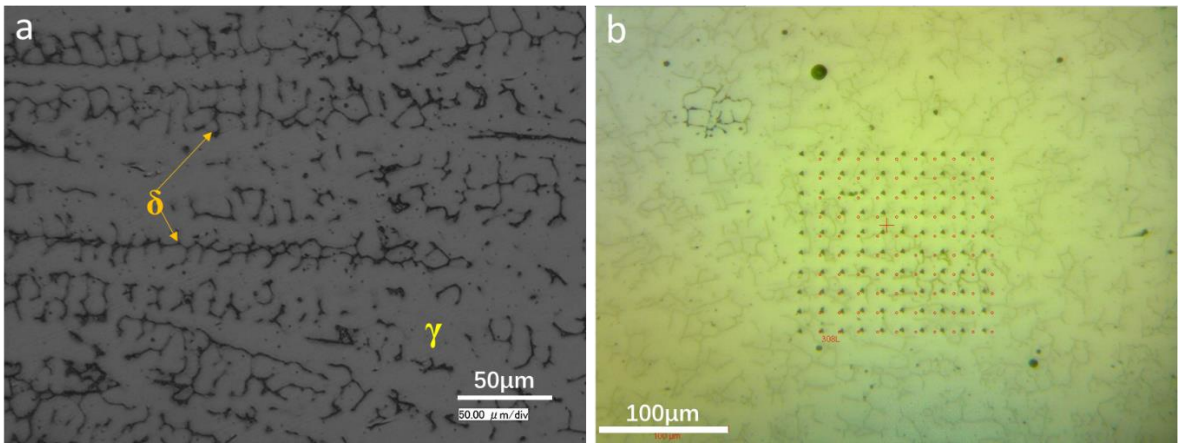

Fig. 1. (a) Optical image of the 308L weld metal after electro-etched in NaOH solution, (b) Nanoindentation test area image of the 308L weld metal.

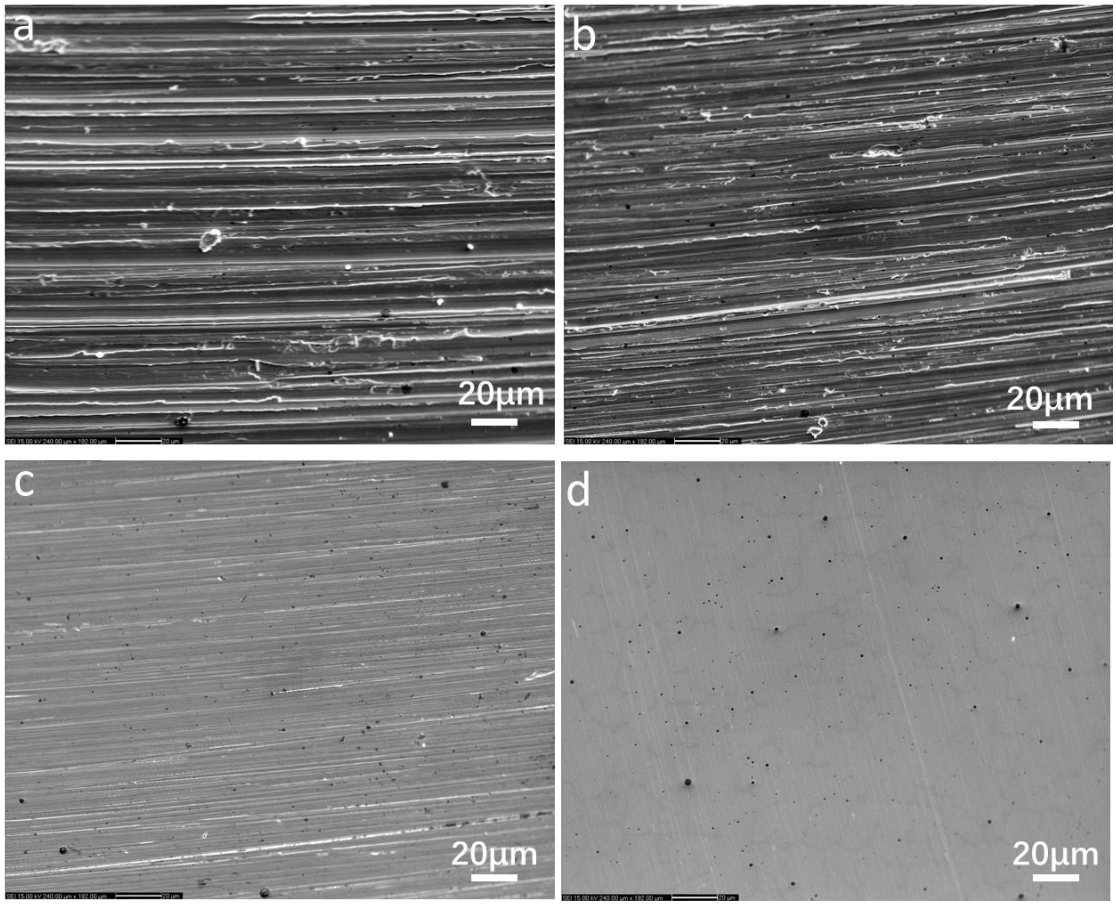

Fig. 2. SEM surface morphology of the 308L SS specimens with different surface treatment: (a) 308-G240, (b) 308-G600, (c) 308-G1500, (d) 308-MP.

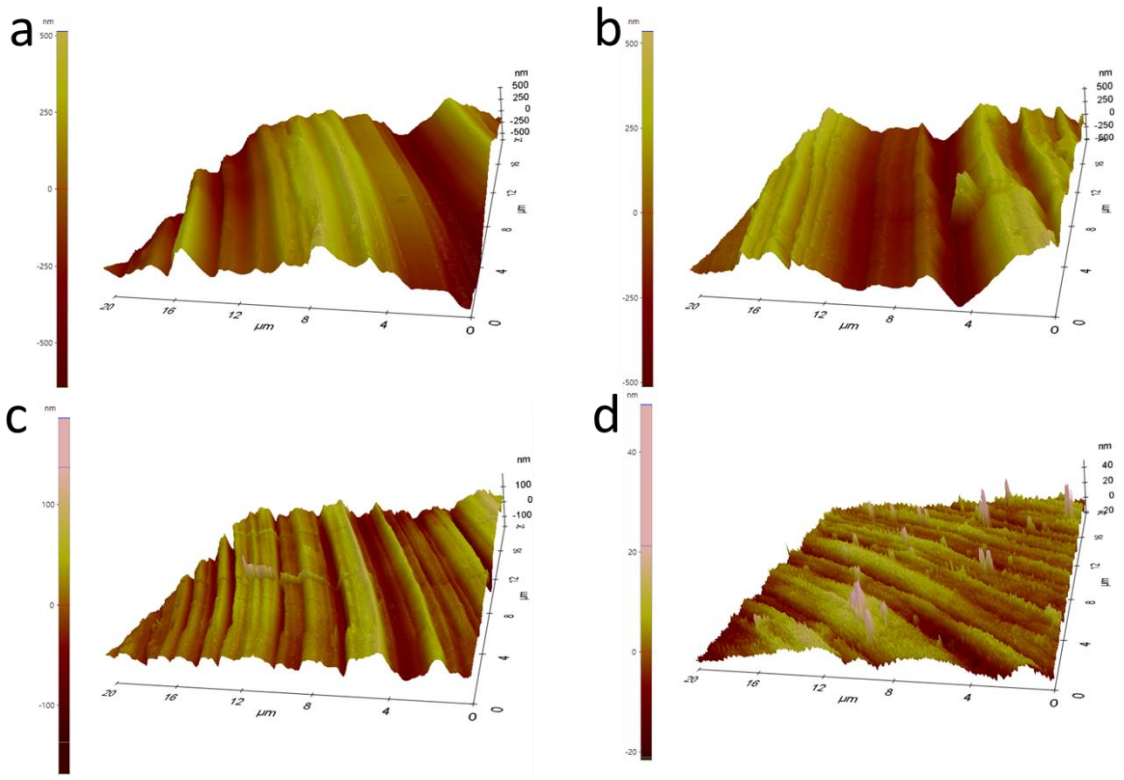

Fig. 3. AFM Topography of the 308L SS specimens with different surface treatment: (a) 308-G240, (b) 308-G600, (c) 308-G1500, (d) 308-MP.

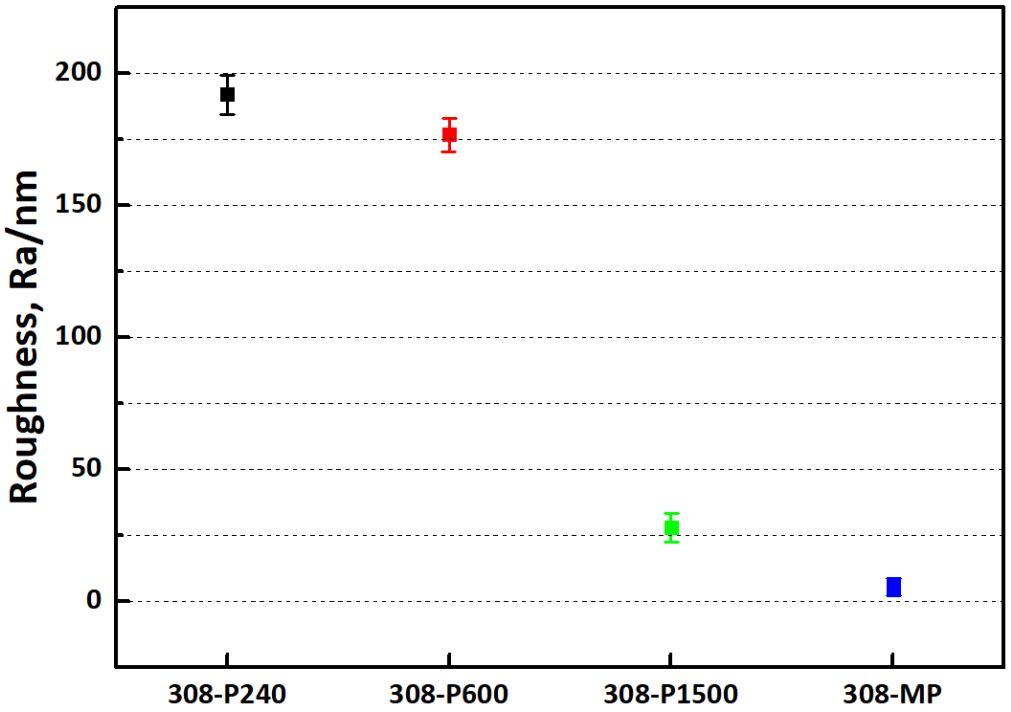

Fig. 4. Roughness values of the 308L SS specimens with different surface treatments.

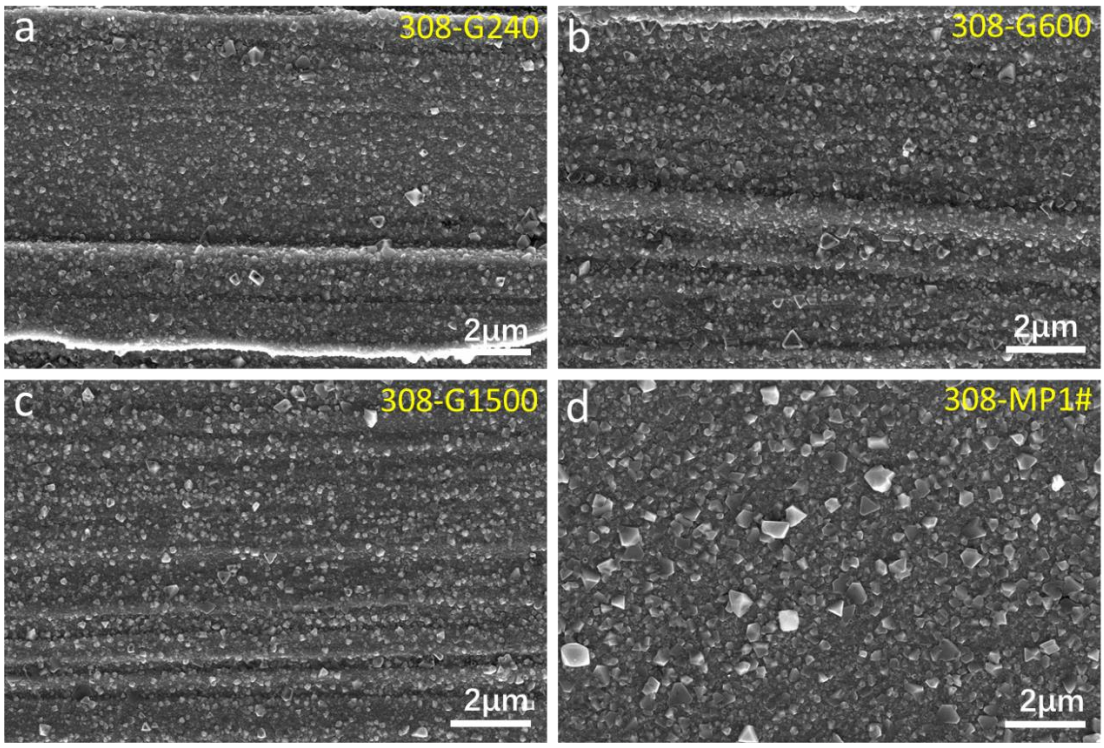

Fig. 5. SEM morphologies of the 308L SS specimens after exposure in hydrogenated simulated PWR primary water at 310 ºC for 616 h: (a) 308-G240, (b) 308-G600, (c) 308-G1500, (d) 308-MP1#.

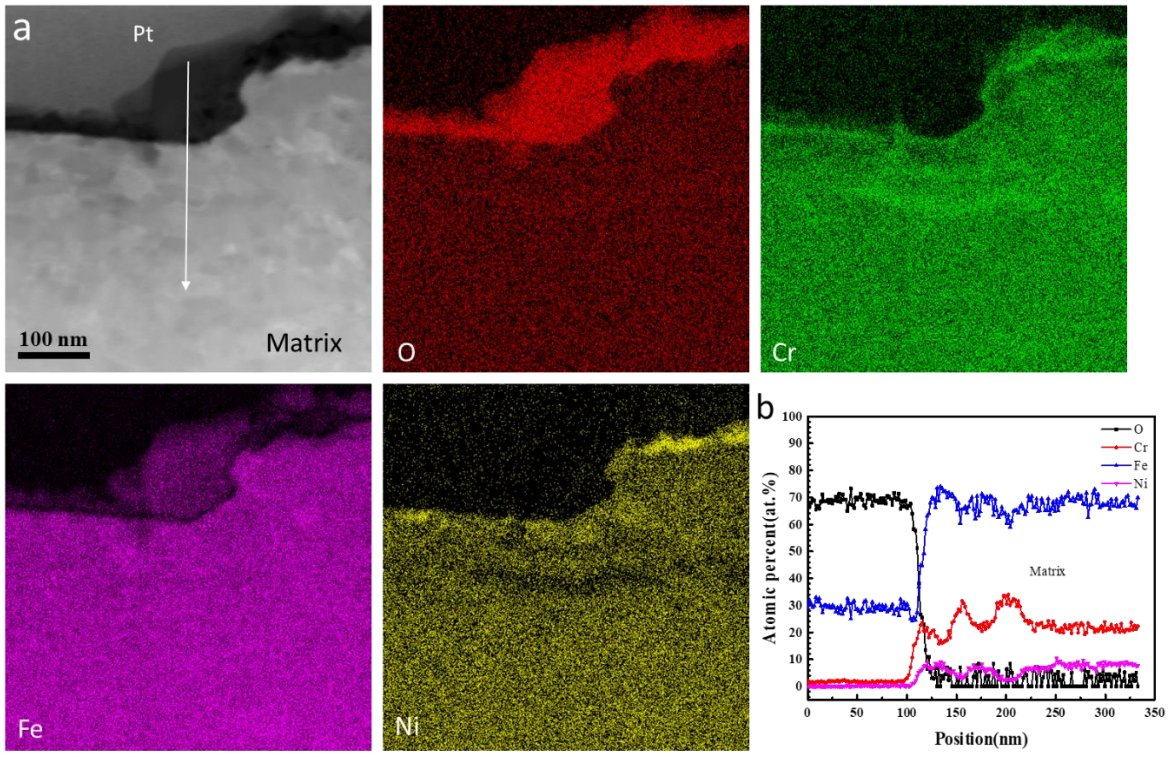

Fig. 6. TEM-EDS results of the oxide film formed on 308-G240 specimen after exposure in hydrogenated PWR primary water at 310 ºC for 616 h: (a) STEM-HAADF image of the oxide film and the corresponding EDS maps, (b) EDS line scan profile of the oxide film shown in (a).

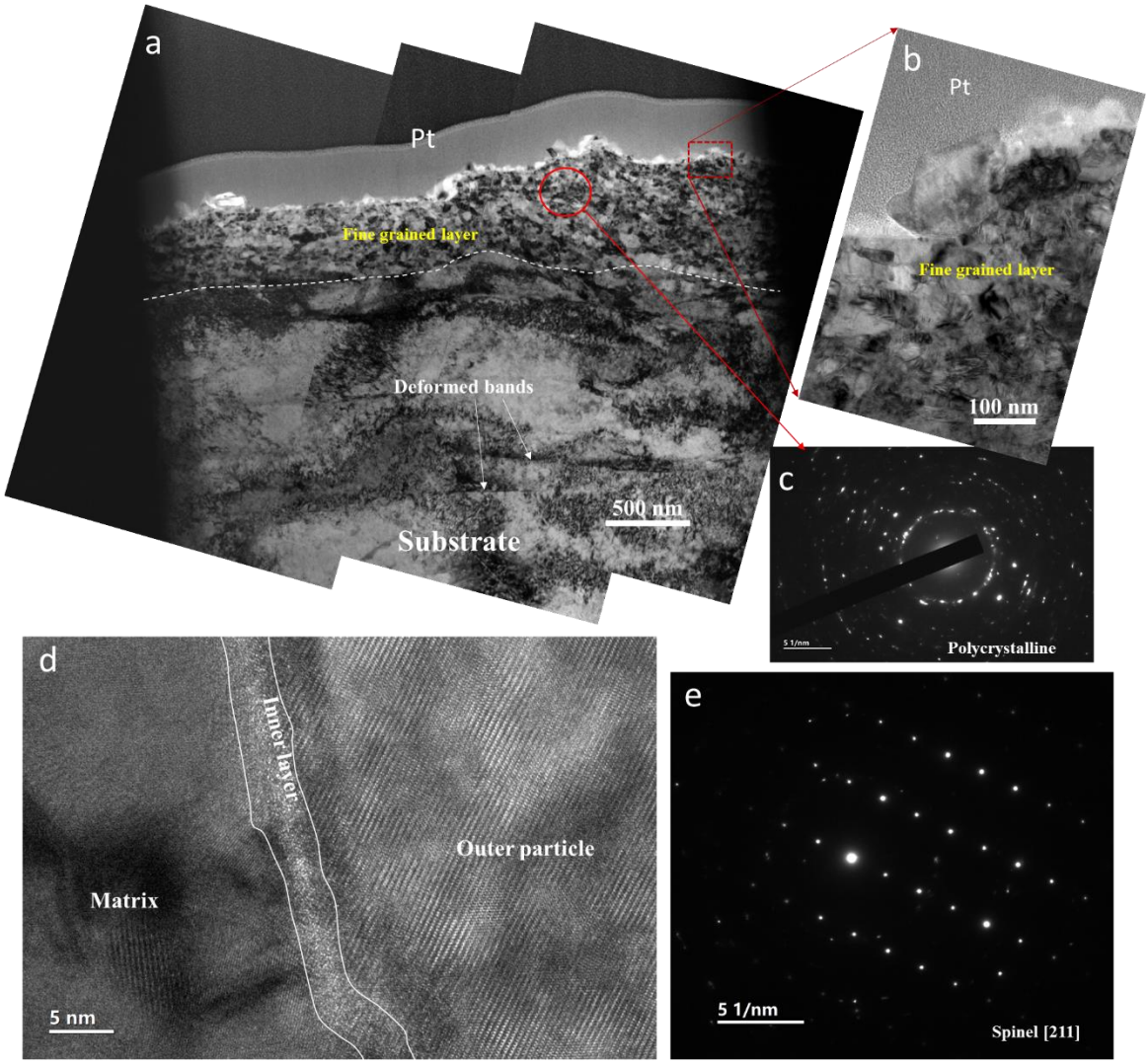

Fig. 7. (a) TEM-BF image of the subsurface and oxide film formed on 308-G240 specimen after exposure in hydrogenated PWR primary water at 310 ºC for 616 h, (b) High magnification TEM-BF image of the fine grained layer marked by the red rectangle dash box shown in (a), (c) SAED image of the fine grained layer as the red circle shown in (a), (d) High resolution TEM image of the outer/inner oxide/matrix interface, (e) SAED pattern of the outer oxide particle.

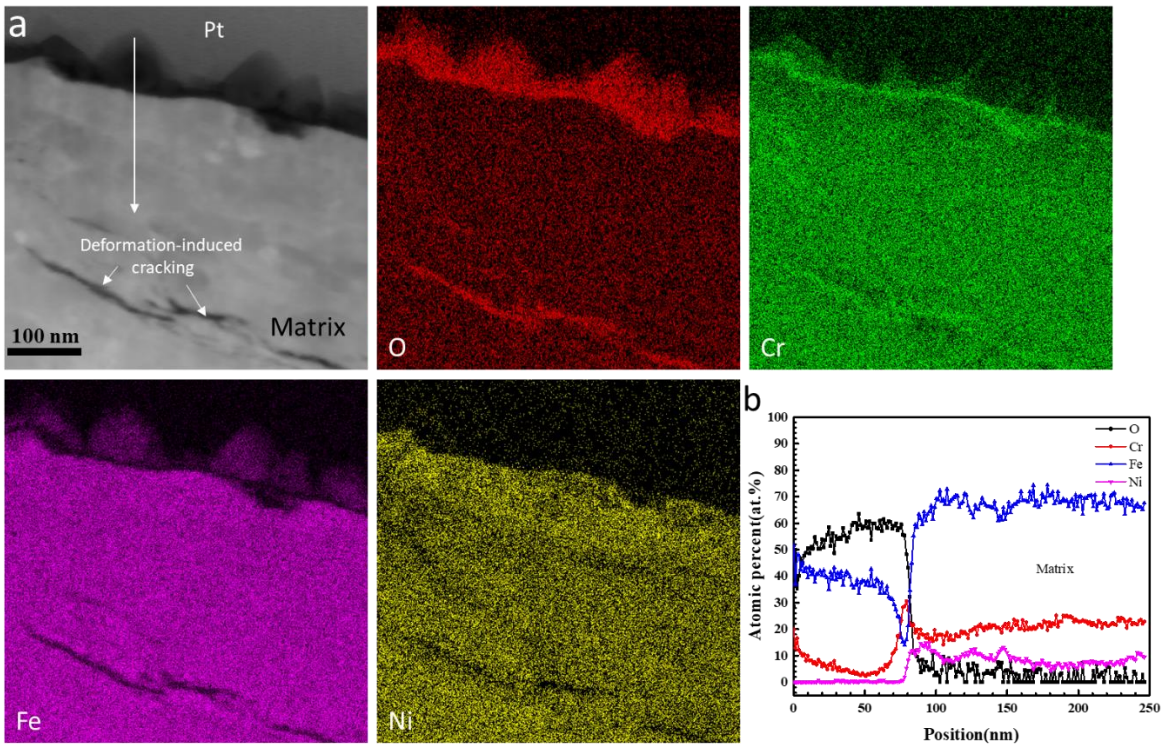

Fig. 8. TEM-EDS results of the oxide film formed on 308-G600 specimen after exposure in hydrogenated PWR primary water at 310 ºC for 616 h: (a) STEM-HAADF image of the oxide film and the corresponding EDS maps, (b) EDS line scan profile of the oxide film shown in (a).

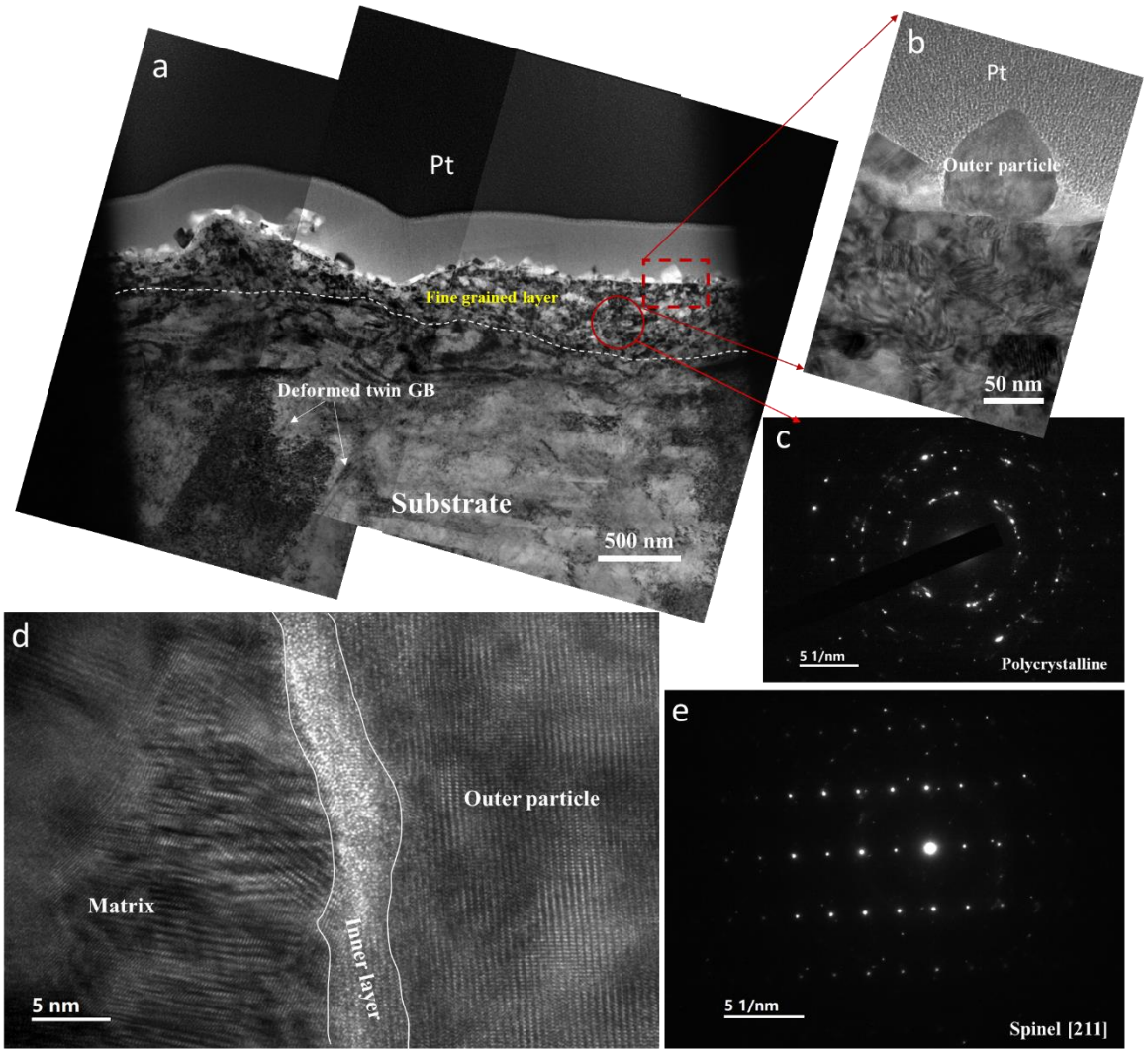

Fig. 9. (a) TEM-BF image of the subsurface and oxide film formed on 308-G600 specimen after exposure in hydrogenated PWR primary water at 310 °C for 616 h, (b) High magnification TEM-BF image of the fine grained layer marked by the red rectangle dash box shown in (a), (c) SAED image of the fine grained layer as the red circle shown in (a), (d) High resolution TEM image of the outer/inner oxide/matrix interface, (e) SAED pattern of the outer oxide particle.

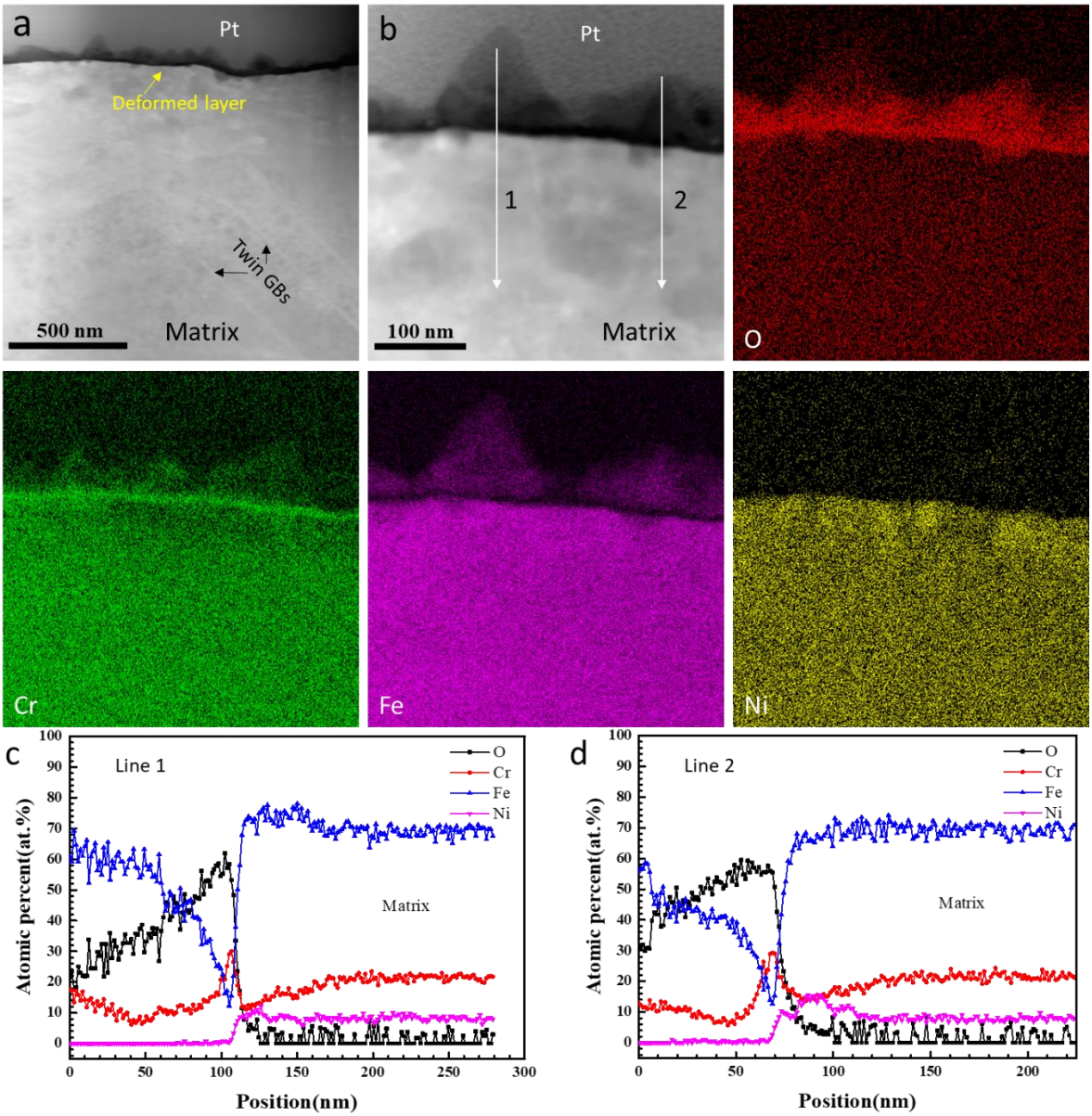

Fig. 10. TEM-EDS results of the oxide film formed on 308-G1500 specimen after exposure in hydrogenated PWR primary water at 310 °C for 616 h: (a) Low magnification STEM-HAADF image of the oxide film, (b) High magnification STEM-HAADF image of the oxide film and the corresponding EDS area maps, (c) EDS line scan profile of the oxide film shown in (a) as line 1, (c) EDS line scan profile of the oxide film shown in (a) as line 2.

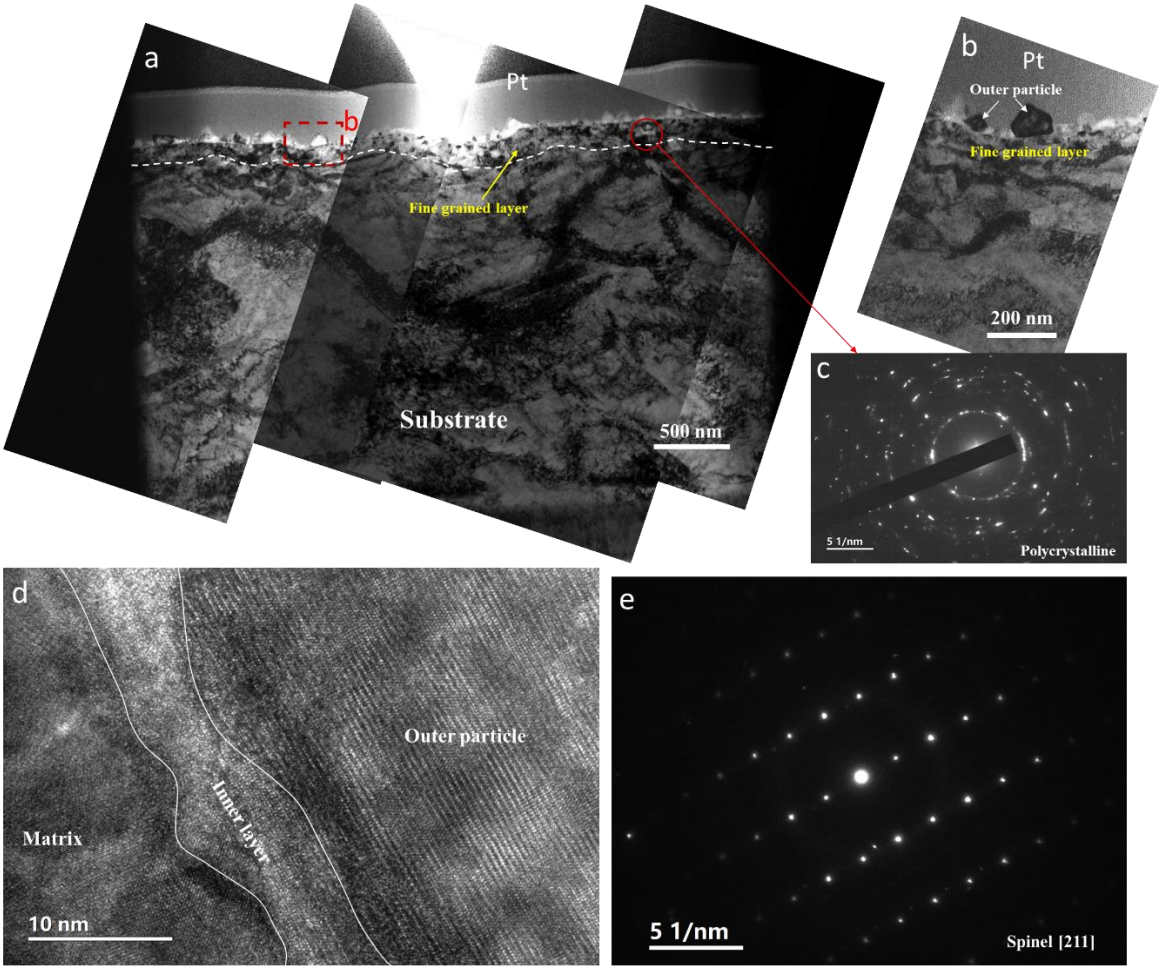

Fig. 11. (a) TEM-BF image of the subsurface and oxide film formed on 308-G1500 specimen after exposure in hydrogenated PWR primary water at 310 ºC for 616 h, (b) High magnification TEM-BF image of the fine grained layer marked by the red rectangle dash box shown in (a), (c) SAED image of the fine grained layer as the red circle shown in (a), (d) High resolution TEM image of the outer/inner oxide/matrix interface, (e) SAED pattern of the outer oxide particle.

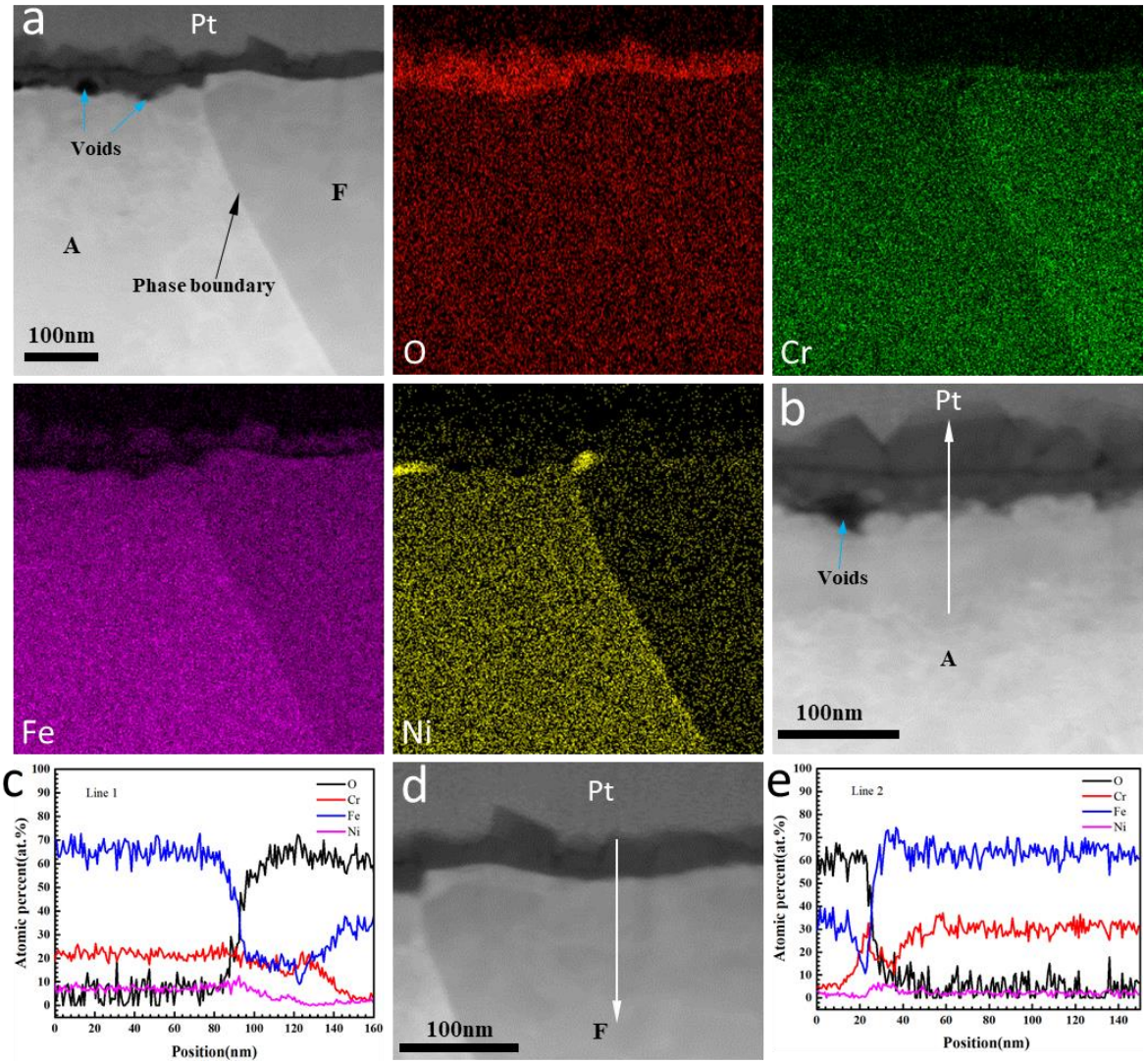

Fig. 12. TEM-EDS results of the oxide film formed near PB on 308-MP1# specimen after exposure in hydrogenated PWR primary water at 310 ºC for 616 h: (a) STEM-HAADF image of the oxide film formed near the phase boundary and the corresponding EDS maps, (b) STEM-HAADF image of the oxide film formed on austenite, (c) EDS line scan profile of the oxide film on austenite shown in (b), (d) STEM-HAADF image of the oxide film formed on ferrite, (e) EDS line scan profile of the oxide film on ferrite shown in (d).

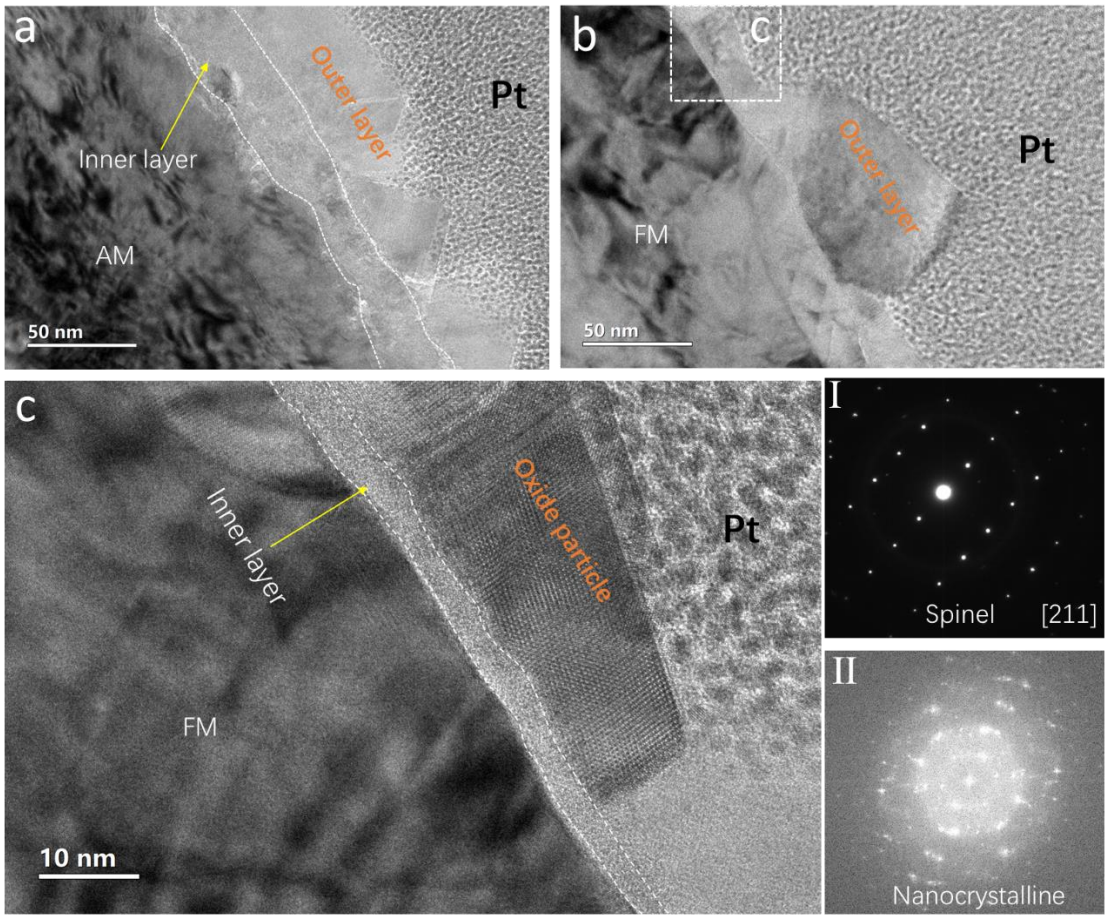

Fig. 13. (a) TEM-BF image of the oxide film formed on austenite in 308-MP1# specimen after exposure in hydrogenated PWR primary water at 310 °C for 616 h, (b) TEM-BF image of the oxide film on ferrite, (c) HRTEM image of the oxide formed on ferrite marked by the white rectangle dash box shown in (b). I shows the SAED pattern of the outer oxide particle on ferrite, II shows the FFT pattern of the inner oxide on ferrite.

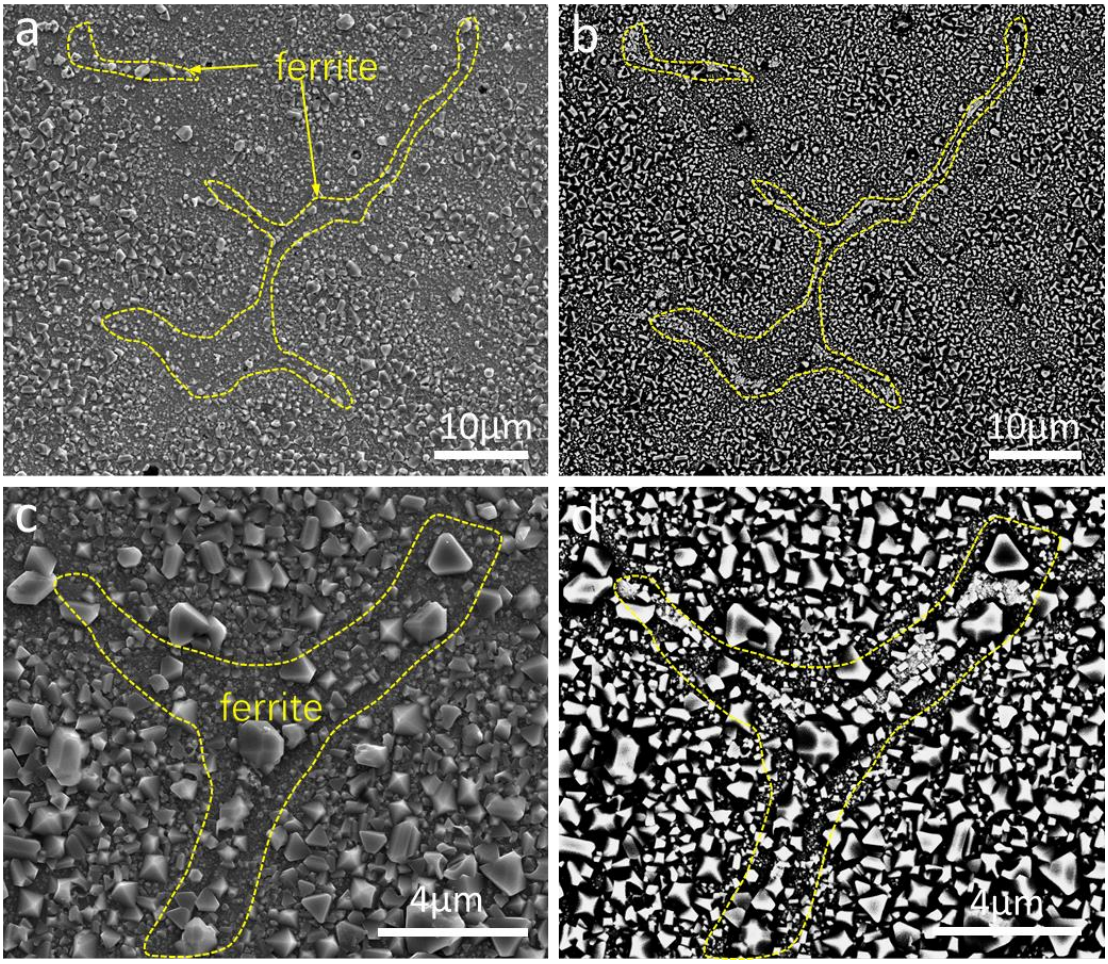

Fig. 14. SEM morphologies of oxide films on 308-MP2# specimen after exposure in hydrogenated PWR primary water at 325 ºC for 1364 h: (a) (c) SE images, (b) (d) BSE images.

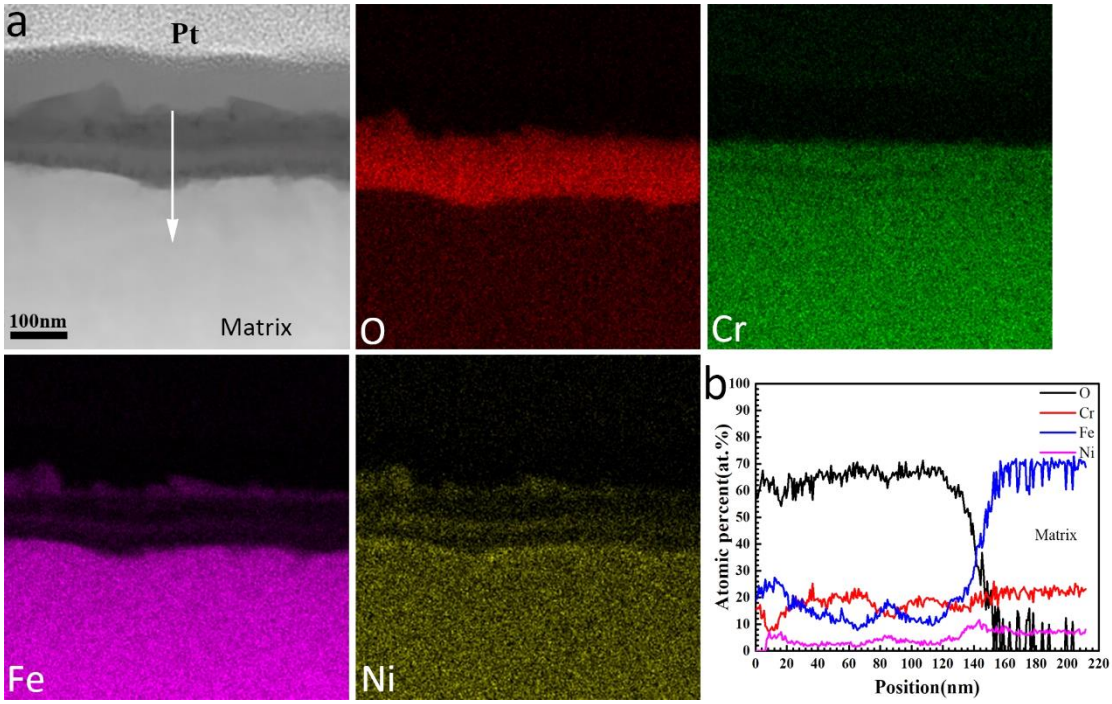

Fig. 15. TEM results of the oxide film formed on austenite in 308-MP2# specimen after exposure in hydrogenated PWR primary water at 325 ºC for 1364 h: (a) STEM-HAADF image of the oxide film on austenite and the corresponding EDS maps, (b) EDS line scan profile of the oxide film on austenite shown in (a).

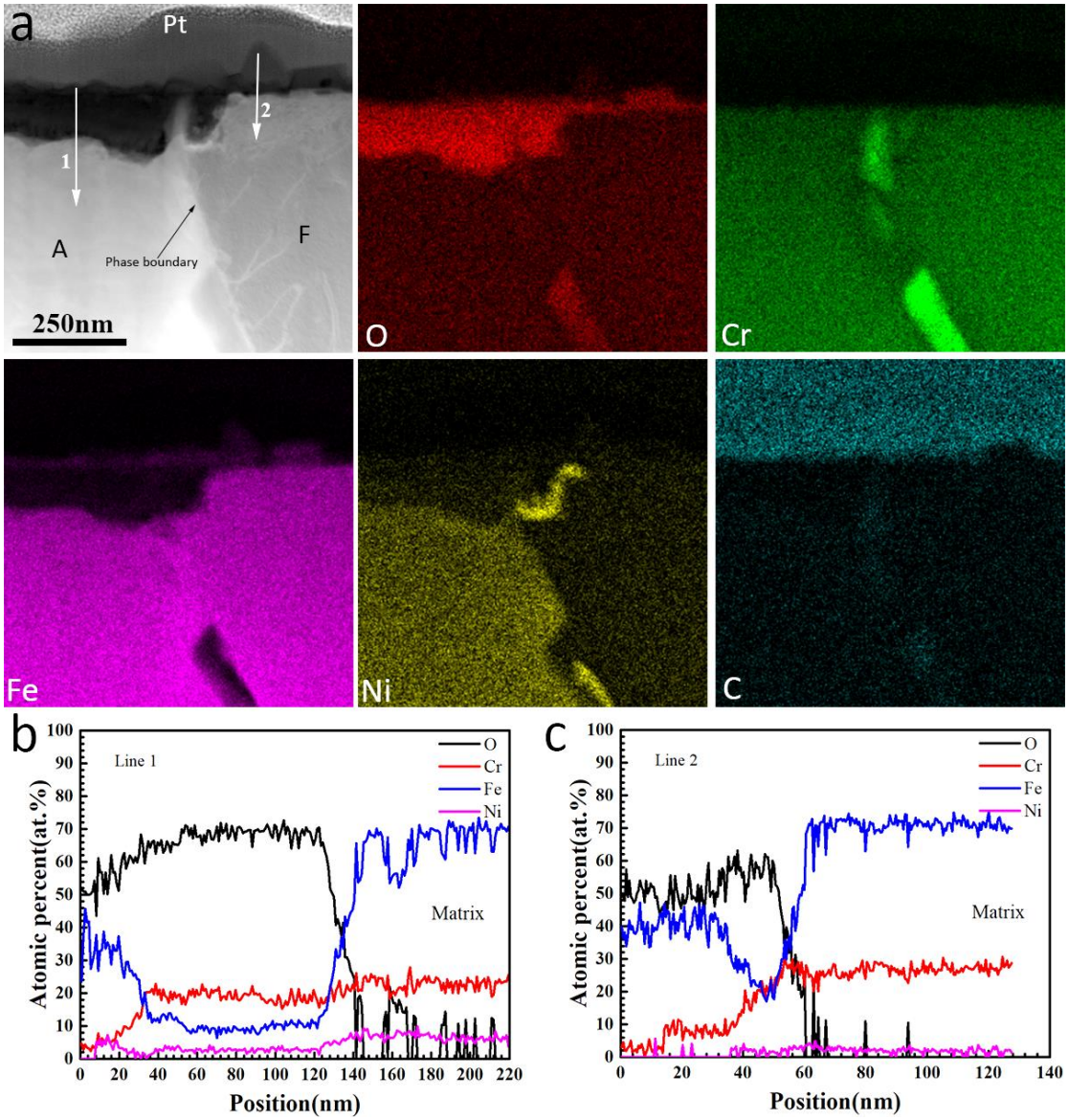

Fig. 16. TEM-EDS results of the oxide film formed near phase boundary on 308-MP2# specimen after exposure in hydrogenated PWR primary water at 325 °C for 1364 h: (a) STEM-HAADF image of the oxide film formed near the phase boundary and the corresponding EDS maps, (b) EDS line scan profile of the oxide film on austenite shown in (a), (c) EDS line scan profile of the oxide film on ferrite shown in (a).

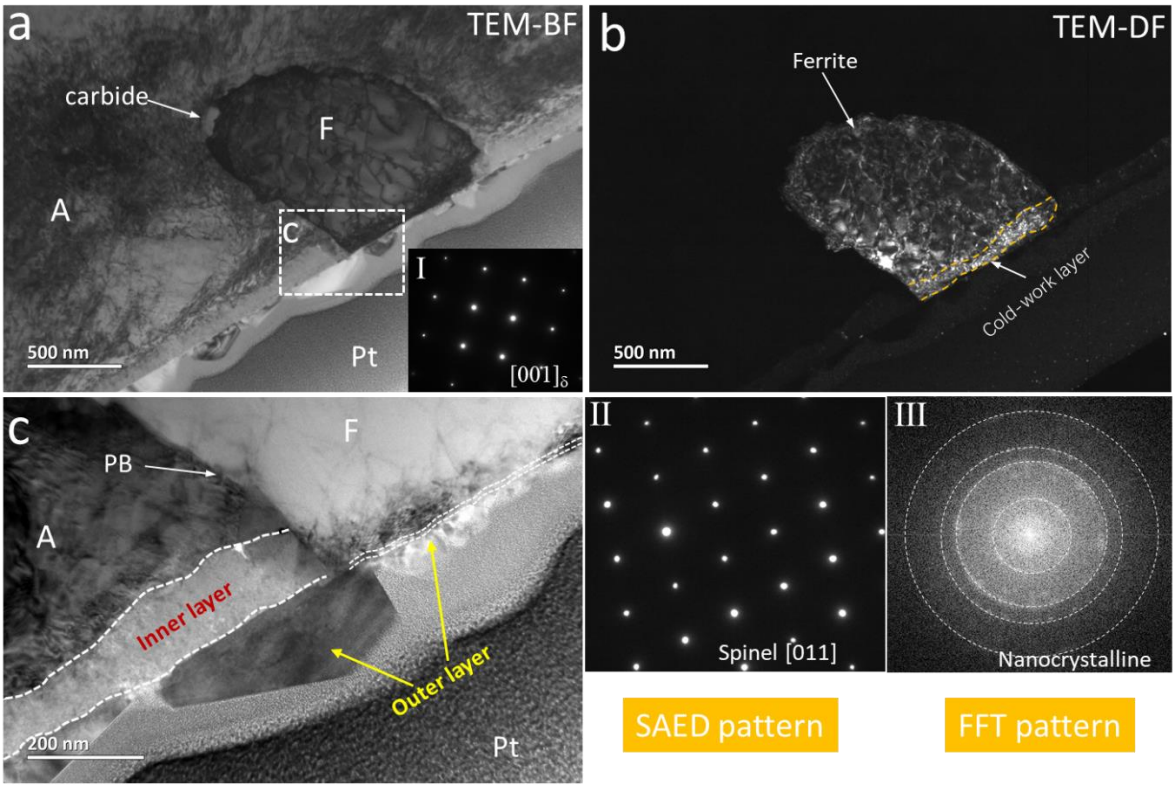

Fig. 17. (a) TEM-BF image of the ferrite and oxide films formed near phase boundary on 308-MP2# specimen after exposure in hydrogenated PWR primary water at 325 ºC for 1364 h, (b) TEM-DF image of the ferrite, (c) High magnification TEM-BF image of the PB and oxide film marked by the white rectangular box shown in (a). I shows the SAED pattern of the ferrite, II shows the SAED pattern of the outer oxide on austenite, III shows the FFT pattern of the inner oxide on austenite.

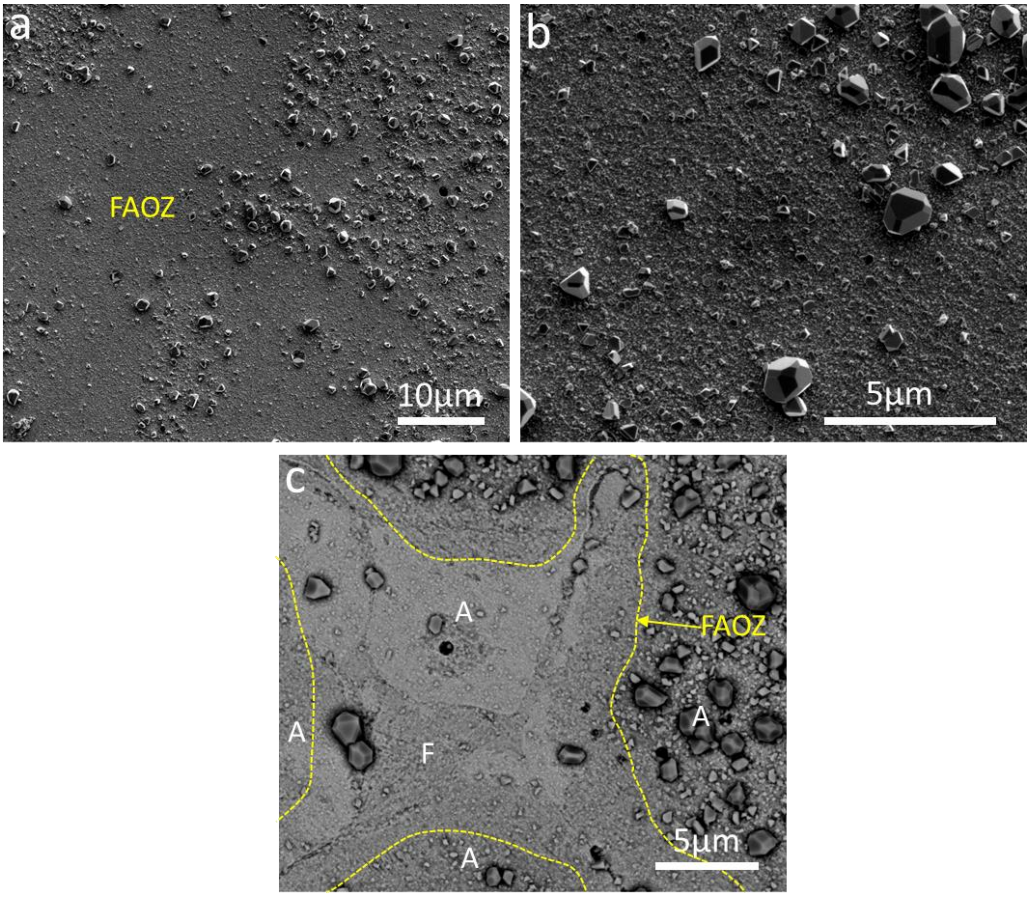

Fig. 18. SEM morphologies of oxide films on 308-MP3# specimen after exposure in hydrogenated PWR primary water at 350 ºC for 930 h: (a) (b) SE image, (c) BSE image.

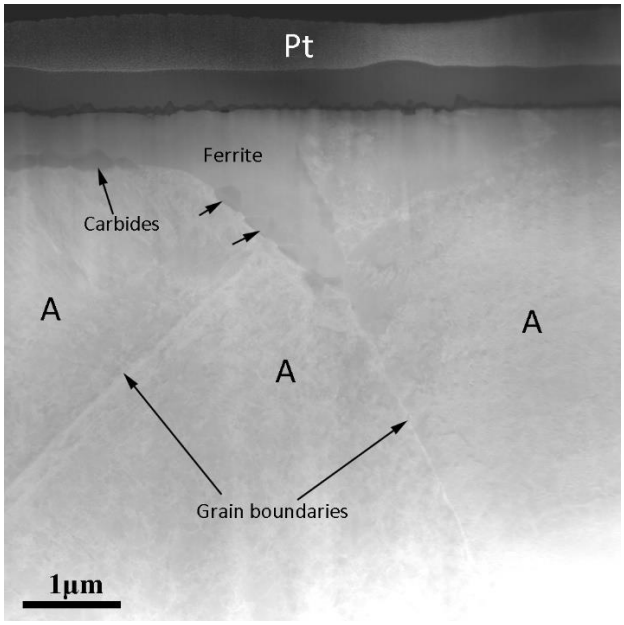

Fig. 19. Low magnification STEM-HAADF image of the oxide film formed on 308-MP3# specimen after exposure in hydrogenated PWR primary water at 350 ℃ for 930 h.

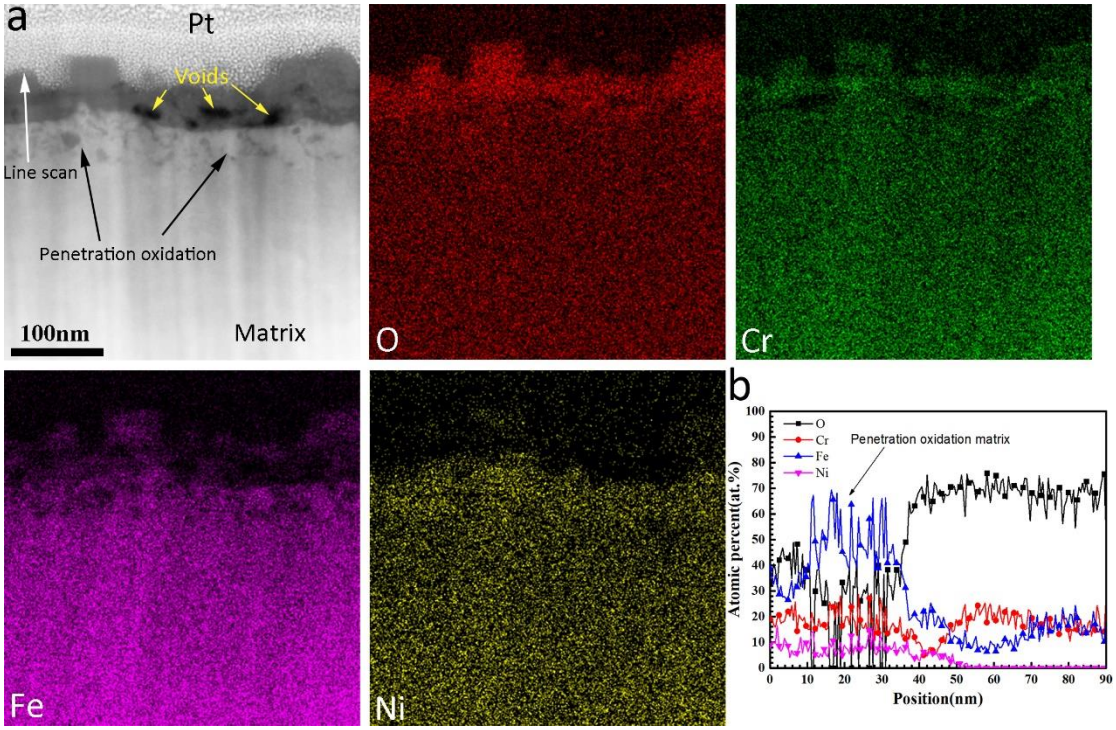

Fig. 20. TEM-EDS results of the oxide film formed on austenite of 308-MP3# specimen after exposure in hydrogenated PWR primary water at 350 °C for 930 h: (a) STEM-HAADF image of the oxide film on austenite and the corresponding EDS maps, (b) EDS line scan profile of the oxide film on austenite shown in (a).

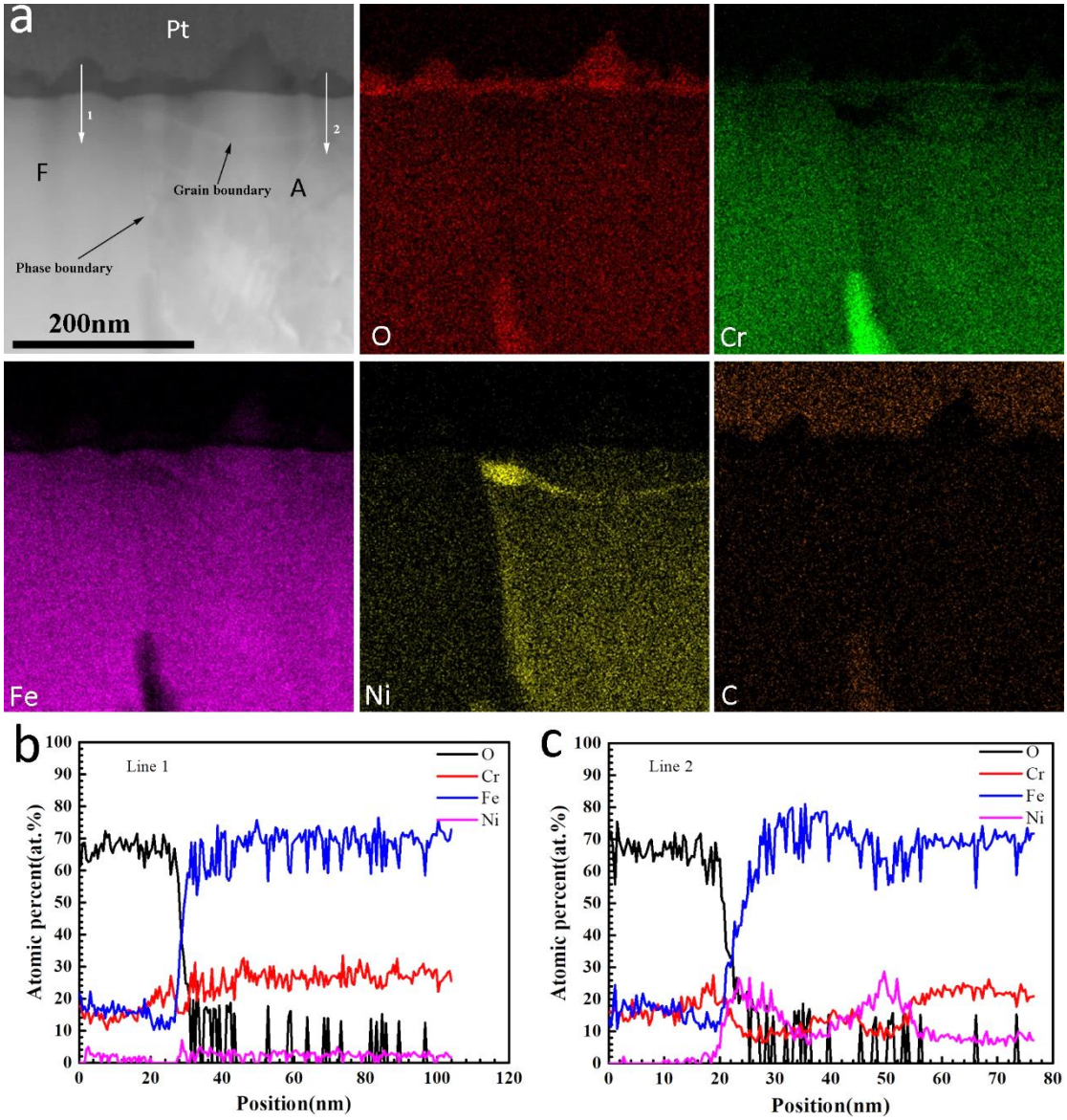

Fig. 21. TEM-EDS results of the oxide film formed near phase boundary (sampling location 1) on 308-MP3# specimen after exposure in hydrogenated PWR primary water at 350 °C for 930 h: (a) STEM-HAADF image of the oxide film formed near the phase boundary and the corresponding EDS area maps, (b) EDS line scan profile of the oxide film on ferrite shown in (a), (c) EDS line scan profile of the oxide film on austenite shown in (a).

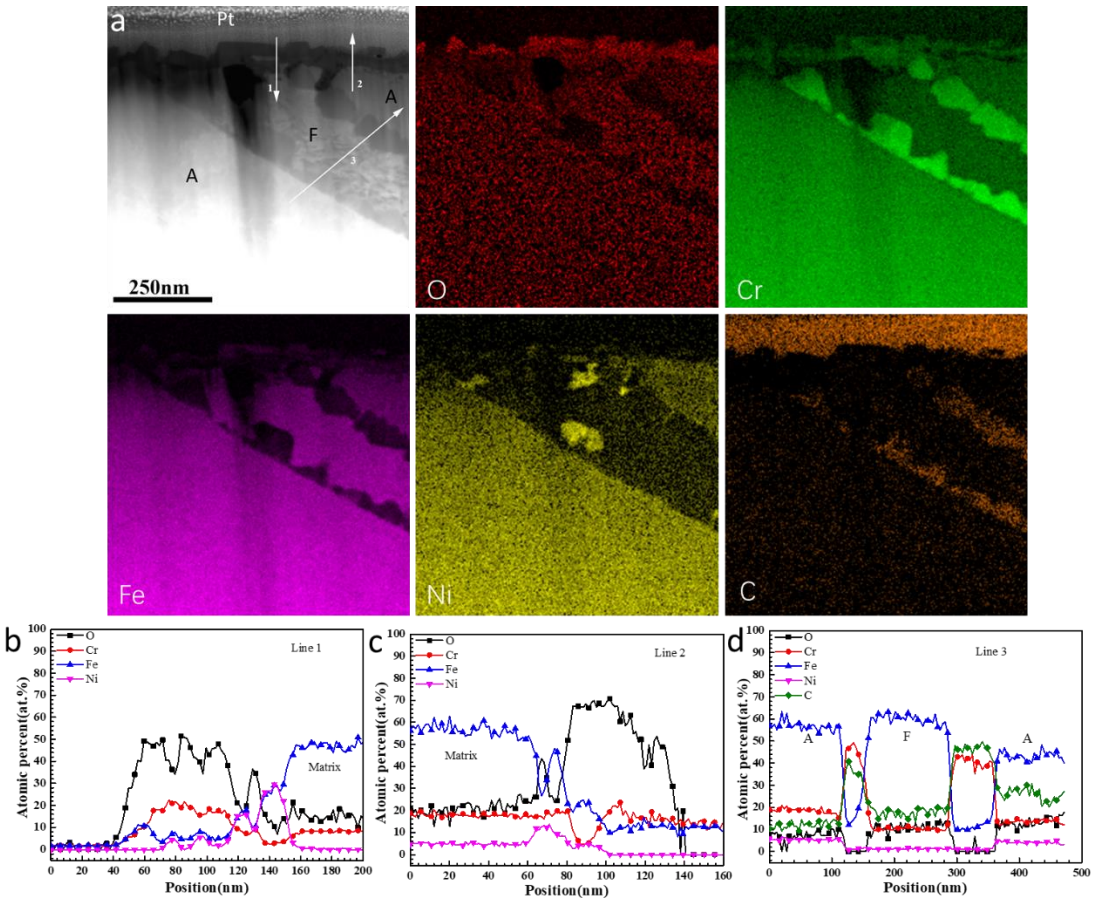

Fig. 22. TEM-EDS results of the oxide film formed near phase boundary (sampling location 2) on 308-MP3# specimen after exposure in hydrogenated PWR primary water at 350 °C for 930 h: (a) STEM-HAADF image of the oxide film formed near the phase boundary and the corresponding EDS area maps, (b) EDS line scan profile of the oxide film on ferrite shown in (a) as line 1, (c) EDS line scan profile of the oxide film on austenite shown in (a) as line 2, EDS line scan profile across the austenite-ferrite-carbide shown in (a) as line 3.

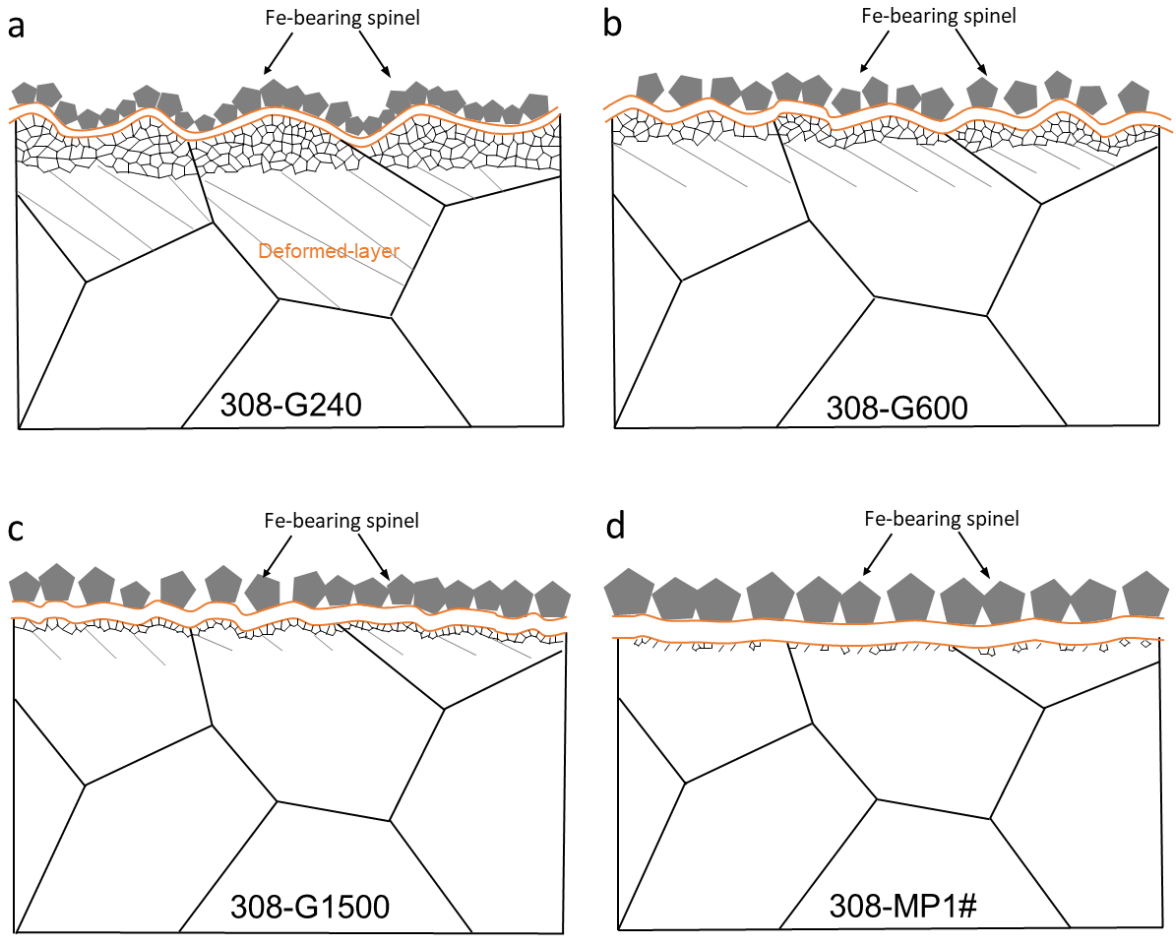

Fig. 23. Schematic diagram of the oxide films grown on a 308L SS cladding (not including PB) with different surface treatments: (a) 308-G240 specimen, (b) 308-G600 specimen, (c) 308-G1500 specimen, (d) 308-MP1#.

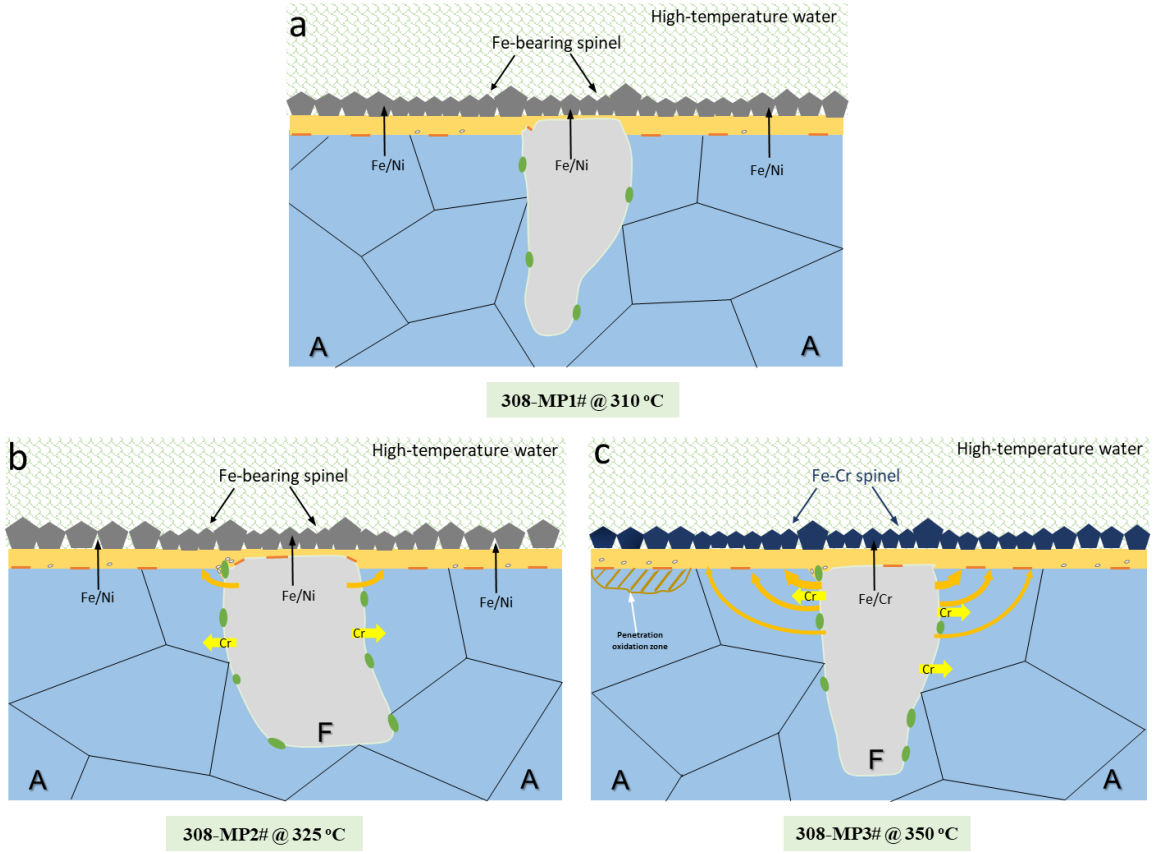

Fig. 24. Schematic diagram of the oxide films grown on mechanical polished 308L SS cladding (including PB) with different temperature: (a) 308-MP1# specimen, (b) 308-MP2# specimen, (c) 308-MP3# specimen. The thickness of the inner oxide layer is arbitrary.

Table 1. Test conditions employed for the oxidation of 308L SS weld metal in simulated PWR primary water.

Sample ID, #	Temperature	Pressure	Exposure time
308-G240 308-G600 308-G1500 308-MP1#	310 °C	12.5 MPa	616 h
308-MP2#	325 °C	13.3 MPa	1364 h
308-MP3#	350 °C	17.2 MPa	930 h

Table 2. Summary of the near-surface and oxide films properties of 308L SS weld metal with various surface states in simulated PWR primary water.

Sample ID, #	Fine-grained layer Thickness (nm)	Inner oxide layer Thickness (nm)	Oxide film composition
308-G240	600±100	5±1	Fe-outer, Cr-inner
308-G600	400±150	7±1	Fe-outer, Cr-inner
308-G1500	200±50	9±2	Fe-outer, Cr-inner
308-MP1#	No fined-grained layer, only deformed layer	40±5 on AM ⩽10 nm on FM	Fe-outer, Cr-inner
308-MP2#	/	85±10 on AM 20±3 nm on FM	Fe-outer, Cr-inner
308-MP3#	/	/	Fe-Cr outer, Cr-inner